J. Fluid Mech. (2004), *vol.* 512, *pp.* 153–189.
DOI: 10.1017/S0022112004009553 Printed in the United Kingdom

The optical distortion mechanism in a nearly incompressible free shear layer

By E. J. FITZGERALD† AND E. J. JUMPER

Department of Aerospace & Mechanical Engineering, University of Notre Dame, Notre Dame, IN 46556, USA

(Received 16 October 2001 and in revised form 17 March 2004)

The aero-optical distortions caused by compressible flows have been used by researchers for flow diagnostics and accepted by designers of airborne optical systems as a performance penalty. In order to estimate these distortions, an understanding of the optical distortion mechanism is required. This article examines the mechanisms which produce a variable-density field (and accompanying index-of-refraction field) in a nearly incompressible shear-layer flow. The two-dimensional-shear-layer velocity field was approximated using a discrete vortex model. From this 'known' velocity field, the pressure and density fields were determined by iteratively solving the unsteady Euler equations. The resulting index-of-refraction field produced simulated schlieren images which closely resemble experimental schlierens. Optical wavefronts computed from the simulation reasonably match the behaviour of large-scale aberrations measured in a transonic wind tunnel. Small-scale distortions in the experimental data may have been caused by boundary layers on the splitter plate and tunnel walls or by three-dimensional effects that were not simulated.

1. Introduction

The transmission of a collimated beam of light through a turbulent variable-index-of-refraction flow (caused by temperature or density variations, for example) produces a time-varying distortion on the previously planar optical wavefront. When the depth of the turbulent region is on the same order as the beam aperture or less, the phenomenon is termed 'aero-optics' (Gilbert 1982). The aberrating flow fields in the near field are usually associated with propagation through turbulent shear and boundary layers. The high propagation speed of light relative to practical flow speeds means that the optical beam sees a ('slowly' time-varying) series of 'frozen' index-of-refraction fields. Thus the aero-optic problem is inherently tied to the dynamics of the flow field.

1.1. *Aero-optics fundamentals*

The first users of aero-optics information were fluid mechanics researchers who took advantage of the variable index of refraction that accompanies variable-density flows. Schlieren and shadowgraph systems have traditionally provided a mostly qualitative measure of flow-field aberrations and the flow that produced them. Interferometric techniques, on the other hand, are capable of very sensitive quantitative measures of

† Present address: The Boeing Company, 13100 Space Center Blvd., MC HZ1-10, Houston, TX 77059-3556, USA.

the variation in the beam's optical path length (OPL) as it traverses the flow. The (instantaneous one-dimensional) optical path length is defined by

$$OPL(t, x) = \int_{y_1}^{y_2} n(t, x, y)\,\mathrm{d}y \tag{1.1}$$

where $n(t, x, y)$ is the index of refraction field along the (constant-x) path that the beam travels (y_1 to y_2). Since, for air and most homogeneous gases, the index of refraction is linearly related to the flow density, ρ (Goldstein 1983), a variable-density flow is required to produce an optical aberration. In practice, rather than measuring an (instantaneous) absolute OPL, the interferometer is used to measure the relative difference in OPL across the aperture or optical path difference (OPD) defined as

$$OPD(t = t_0, x) = OPL(t = t_0, x) - \overline{OPL}(t_0), \tag{1.2}$$

where the overbar denotes the spatial average over the aperture. It can be shown (see Hugo 1995, for example) that the OPD is the conjugate (or inverse) of the optical wavefront.

Also concerned with aero-optics are the designers of optical systems that must look through variable-refractive-index flows. Such systems include missiles with optical seekers, airborne telescopes, airborne laser communication platforms, and airborne laser weapon systems. For systems like these, optical aberrations translate directly into reductions in system performance. In general, the overall aero-optical effect can be produced by several contributions, any of which can produce local density gradients. In practice these include high-speed shear flows, separated flows, shocks, and local flow accelerations produced by streamwise pressure gradients (Gilbert 1982). High-Mach-number applications may also involve heat transfer effects or cooler, often dissimilar-index fluids, used to cool exposed optical elements (Holden *et al.* 2000). For all but the missile applications, the maximum flow Mach numbers involved are approximately 0.6–1.0. The dominant unsteady cause of aero-optic distortions in these cases is typically a turbulent boundary or shear layer composed of a single constituent fluid (air, for example); in the case of a shear layer, both streams are likely to share a common total temperature, T_0, and to be static-pressure matched. Aero-optics researchers have generally attributed the cause of the optical distortions in this sort of flow to 'compressibility' since velocity-related density differences are at work. This is despite the fact that many fluid mechanics researchers would consider such subsonic flows to be essentially incompressible. This article will focus on such a high-subsonic-Mach-number shear-layer flow.

Through the mid-1980s, the optical-system design approach was to attempt to estimate the root-mean-square (r.m.s.) OPD degradation and develop a system which could accept these losses (Jumper & Fitzgerald 2001). It has since been shown that such methods can underpredict the aberrations produced by flows containing coherent structures (Cicchiello & Jumper 1997). Now the research community is considering the possibility of improving a system's performance either by modifying the flow field to reduce the distortion (Chew & Christiansen 1991) or by applying a real-time correction using adaptive optics (Cicchiello & Jumper 1997). In any case, there is a need to predict and characterize aero-optic aberrations during the system's design phase. Such predictions require an understanding of the fundamental flow mechanisms which cause these optical distortions.

Prior to the present study, much work in aero-optics has involved low-speed optically active flows. Until the development of the small-aperture beam technique (SABT) sensor (Jumper & Hugo 1995), a device based on the realization by

Malley, Sutton & Kincheloe (1992) that aero-optical aberrations convect with flow structures, wavefront sensors with sufficient bandwidth for time-resolved time-series measurements in transonic flows were unavailable. Thus, many previous researchers (e.g. de Jonckheere *et al.* 1988; Chew & Christiansen 1991, 1993; Brooke *et al.* 1996; McMackin *et al.* 1995; Masson *et al.* 1995; Jumper & Hugo 1995; Hugo & Jumper 1996; Hugo & McMackin 1996; McMackin *et al.* 1997; Luna, Truman & Masson 1997; Oljaca & Glezer 1997) have found dissimilar-index incompressible flows as the practical choice for studying aero-optical effects. Likewise, numerical computations of aero-optics using the compressible Euler equations have been run at Mach numbers below ≈ 0.2 (Tsai & Christiansen 1990), presumably to reduce the computational requirements and/or to match a specific laboratory experiment.

Dimotakis, Catrakis & Fourgette (2001) used a similar approach to experimentally study aero-optical distortions created by shear layers with convective Mach numbers $M_{c1} = 0.15, 0.54,$ and 0.96. Their shear layers were produced with helium or nitrogen as the higher-speed flow mixing with a lower-speed ethylene flow. While the ethylene and nitrogen were density-matched, the ethylene produced good Rayleigh scattering of a laser light sheet projected through the flow. Photographs of the resulting flow visualization effectively gave the instantaneous number density of ethylene in the flow field. From the number density field, the index field could be deduced, and Dimotakis *et al.* (2001) could compute the resulting wavefront distortion. Their reliance on the number density of ethylene, however, while clearly incorporating Mach effects on *mixing*, does not allow insight into the effects of velocity variations *alone* on wavefront distortion.

Although such two-index flows are not strictly valid for the case considered in this article, the similarities between the coherent structures in, e.g., incompressible and compressible mixing layers (Brown & Roshko 1974; Papamoschou & Roshko 1986, respectively) make it tempting to draw the conclusion that two-index flow experiments might also be applied to their compressible single-constituent-fluid counterparts. In fact, some researchers have already explicitly assumed this to be possible (Cicchiello & Jumper 1997; Gardner *et al.* 1995). Others have implicitly made this assumption. Chew & Christiansen (1991, 1993), for example, pointed to 'compressibility'-caused aero-optics as a research motivation while performing low-speed experiments. Tsai & Christiansen (1990) used a compressible Euler code to study the time-resolved aero-optics of a $M = 0.2$ shear layer. Since velocity-caused density differences at this Mach number are negligible, their code modelled the mixing of constituent air streams at two different densities, thereby producing a mixture of fluids with different initial index of refraction. In their article, Dimotakis *et al.* (2001) proposed a beam-propagation model in which the shear-layer index field is defined by three regions: the two outer streams at their respective indices of refraction and the mixed region at a (weighted) average of the two source indices. As will be discussed below, velocity fluctuations and streamline curvature can produce greater variation in index than a two-index model would suggest (with accompanying increases in wavefront distortion). A table illustrating these differences will be presented in § 5.1.

One approach to computing the aero-optical aberration produced by a high-subsonic-Mach-number shear layer would be to solve the unsteady Euler or Navier–Stokes equations. A time series of realizations of the shear-layer density field could be found using methods like those of Leep, Dutton & Burr (1993); Sandham & Reynolds (1990, 1991); Vreman, Guerts & Kuerten (1997) (temporally developing shear layers) or Hedges & Eberhardt (1993); Oh & Loth (1995); Liou, Lien & Hwang (1995) (spatially developing shear layers). This approach yields a solution for the tested

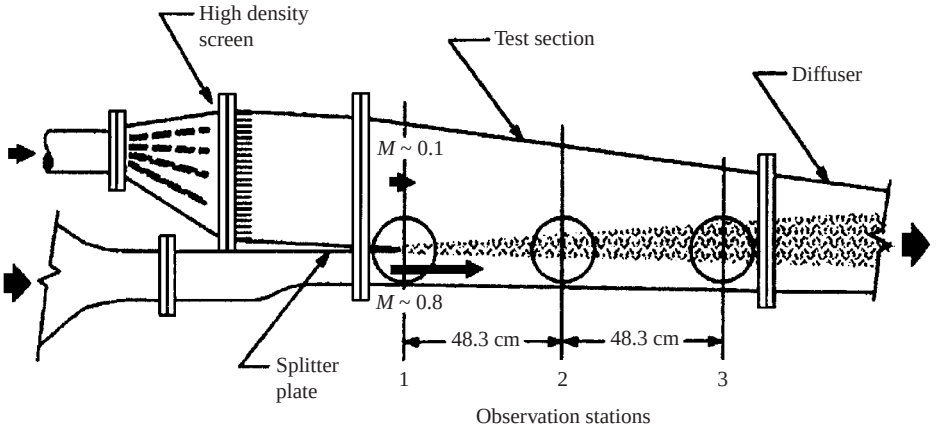

FIGURE 1. Schematic of AEDC test section, from Hugo *et al.* (1997).

conditions only, providing little insight into how the density field (and ultimately *OPD*) will vary with changing initial/boundary conditions or the actual mechanism(s) causing the density changes. Such insight can only be gained in this approach through systematic parametric studies. An alternative to this brute-force approach is to formulate a first-order theoretical model. Such a model has less ambiguity about physical causes and effects, and its simplicity allows multiple cases to be quickly analysed. This latter approach was followed for the present research. A simplified multiple-mechanism model was generated by considering the assumed most-probable contributors and comparing the resulting optical aberrations to observation (in this case the experimental data obtained by Hugo *et al.* 1995, 1997, in a 0.8-Mach shear layer).

The next section describes the Hugo *et al.* (1997) experiment, performed at Arnold Engineering Development Centre (AEDC). In subsequent sections, first-order compressibility mechanisms will be explored using a two-dimensional numerical flow simulation that provided a common, time-varying, velocity field. After describing the numerical model, the results of each overlaid physical mechanism will be compared to the experimentally measured wavefronts.

2. AEDC weakly compressible-shear-layer experiment

The first time-resolved time-series measurements of optical wavefronts in a high-subsonic-Mach-number shear layer were performed by Hugo *et al.* (1997). These measurements were made in the modified Acoustic Research Tunnel located at AEDC using the SABT wavefront sensor. The AEDC shear layer was produced from a ≈ 0.8 Mach high-speed side mixing with ≈ 0.1 Mach low-speed side as shown schematically in figure 1. The experiment's high velocity ratio produced a high entrainment rate and required the tunnel's area to contract in order to maintain a zero pressure gradient. The shear-layer splitter plate was planar and uniform in the spanwise direction. For these tests, the unit Reynolds numbers for the slow and fast streams were 1.4 and $12.7 \times 10^6\ \mathrm{m}^{-1}$, respectively. As each stream was supplied from a common plenum, they shared a common total temperature, $T_0 \approx 27\,^{\circ}\mathrm{C}$. The static pressure across the shear layer was constant and equal to the stream-matched static pressure, ≈ 0.6 atm (Havener & Heltsley 1994).

The test section had three observation stations. The first was centred on the trailing edge of the splitter plate, and the remaining two were spaced 48.3 cm successively downstream. Each station consisted of four viewing windows. Two were on either side of the facility for viewing along the span of the splitter plate (as shown in figure 1). The remaining two windows per station, one on top, the other on the bottom, allowed optical access normal to the splitter plate. Hugo *et al.* (1997) used the SABT sensor (Jumper & Hugo 1995) to measure one-dimensional optical wavefronts through these latter windows. A more detailed description of the facility is given by Havener & Heltsley (1994).

The flow in the AEDC facility was 'compressible' at least in the sense that density variations did exist. The required fidelity of the model needed to simulate the AEDC flow field is ultimately dependent on how 'compressible' the experimental flow was. Shear layer 'compressibility' can be characterized by the convective Mach number M_{c1} of the largest flow structures. M_{c1} is defined as (Papamoschou & Roshko 1988)

$$M_{c1} = (U_1 - U_c)/a_1 \tag{2.1}$$

where U is the velocity in the x-direction and the convection velocity U_c is given by

$$U_c = \frac{a_2 U_1 + a_1 U_2}{a_1 + a_2}, \tag{2.2}$$

where a is the sonic speed, and 1 and 2 refer to the high- and low-speed streams, respectively. For the conditions tested by Hugo *et al.* (1997) at AEDC, the high-speed side of the shear layer was only $M_1 = 0.8$; this means there were no shocks in the flow. Additionally, with a low-speed side of 0.1 Mach, the convective Mach number seen by the largest-scale two-dimensional coherent flow structures would be only $M_{c1} \approx 0.33$ for this case (Papamoschou & Roshko 1986; Havener & Heltsley 1994). The incompressible shear layer's spreading rate can be defined in terms of the growth with increasing x of the vorticity thickness given by (Brown & Roshko 1974)

$$\delta_\omega = \frac{U_1 - U_2}{(\partial U/\partial y)_{max}}. \tag{2.3}$$

The vorticity thickness spreading rate, δ_ω/x, for the AEDC M_{c1} actually remains unchanged from the incompressible case (Papamoschou & Roshko 1986). Other measures of the shear-layer thickness have shown $< 10\%$ reduction in spreading rate for the AEDC conditions (Papamoschou & Roshko 1986; Hall, Dimotakis & Rosemann 1993).

Another measure of the compressibility is the fluctuating divergence, $\nabla \cdot \boldsymbol{u}'$, where $\boldsymbol{u}'$ is the fluctuating portion of the flow velocity resulting from a Reynolds-type decomposition. According to Smits & Dussauge (1996), the ratio of the fluctuating divergence to the magnitude of the velocity gradients of the energy-containing eddies, u'/Λ, is given by

$$\frac{\nabla \cdot \boldsymbol{u}'}{u'/\Lambda} \approx 10(\gamma - 1)M_t^2 \tag{2.4}$$

where γ is the ratio of specific heats for the gas, $M_t = (\overline{u'^2})^{1/2}/\bar{a}$ is the turbulent Mach number, and overbars signify time averages. For an AEDC-like flow field, $M_t \approx 0.09$ whereby

$$\frac{\nabla \cdot \boldsymbol{u}'}{u'/\Lambda} \approx 0.03 \ll 1, \tag{2.5}$$

suggesting that the compressibility is weak and the fluctuating divergence might be neglected (Smits & Dussauge 1996; Lele 1994). Since the AEDC flow was only very weakly compressible, it appears that the density effects might reasonably be decoupled from and neglected in the approximation of the velocity field for the AEDC test conditions.

Experimental observations of compressible shear layers, within certain Mach-number restrictions (such as those by Papamoschou & Roshko 1988; Hall *et al.* 1993) have found the flow to be dominated by two-dimensional large-scale vortex structures similar to those found in incompressible shear layers (Brown & Roshko 1974). The planar velocity measurements of Olsen & Dutton (1999) showed that such structures were even present in a (weakly compressible) supersonic shear layer. Additionally, more-complete compressible numerical simulations have shown that changes in the large-scale shear-layer-vortex structure do not occur at low M_{c1} (Sandham & Reynolds 1990, 1991; Leep *et al.* 1993). These suggest that a two-dimensional velocity model that captures the fluid mechanics of incompressible transitionally-turbulent shear layers may reasonably approximate the velocity field of these largest two-dimensional coherent structures.

To investigate the physical mechanisms which produce optical distortions in a subsonic two-dimensional shear layer, optical wavefronts were computed using a two-part numerical model. A time-varying two-dimensional velocity field was computed for the AEDC test conditions. The corresponding density field (and index-of-refraction field) was then modelled using the (input) velocity field. These models are described in detail in the following two sections.

3. Velocity field model

The initial transitionally turbulent flow field in a shear layer is dominated by the shear-layer rollup caused by the inviscid Kelvin–Helmholtz instability mechanism (Thomas 1991). This rollup has been successfully simulated using various inviscid and pseudo-inviscid methods (e.g. Tsai & Christiansen 1990; Ashurst 1979; Inoue 1985; Ghoniem 1990; Liou *et al.* 1995). The shear layer for the present study was modelled using a two-dimensional discrete vortex method (DVM). One of the primary advantages of using a DVM is that it is a reduced-order pseudo-inviscid method. As such, the DVM is able to model the instantaneous shear-layer flow field with a fairly small computational domain, thereby producing considerable computational savings. A second advantage is the simplicity of the DVM model itself. This simplicity allows insight into the cause-and-effect relations of the physics being modelled; such insight was valuable during the development of aero-optical scaling laws reported elsewhere (Fitzgerald & Jumper 2002*b*). DVMs are traditionally applied to fully incompressible flows because they rely on the global influence a discrete vortex induces on the flow field through the Biot-Savart law. Since the AEDC flow was only very weakly compressible (§ 2), a compressible method was not required for the velocity-field model.

It is worth reviewing the extent to which DVMs in general, and the present implementation in particular, properly model two-dimensional incompressible transitionally turbulent shear layers. The DVM technique was first performed by Rosenhead (1932). The method has been subsequently refined using finite-core point (line) vortices (Chorin & Bernard 1973) and redistributing the vorticity by inserting additional vortices as the vorticity-induced velocity fields spread the vortex elements apart (Jumper & Hugo 1995; Beale & Majda 1985; Ghoniem, Heidarinejad & Krishnan 1988). The modern implementations of DVMs are not strictly inviscid

calculations since momentum diffusion can be modelled by a temporal growth in the size of the rotational cores of the discrete vortices (Ashurst 1979; Hugo 1995). The viscous core of each discrete vortex has an initial diameter δ_i that essentially models the vorticity thickness at the splitter-plate trailing edge. More complete discussions of discrete vortex methods are given by Leonard (1980) and by Ghoniem (1990).

The velocity fields for all cases of the present study were produced by a single infinite two-dimensional shear layer modelled with discrete vortices in a manner similar to Jumper & Hugo (1995). The splitter plate and shear layer near the plate trailing edge were modelled by discrete vortices while the influences of vortices far from the plate's trailing edge were modelled analytically. The splitter-plate vortices' positions were indexed by one temporally consistent position which, in effect, kept the splitter-plate configuration fixed; once an individual plate vortex was indexed past the trailing edge, it became another shear-layer vortex and was allowed to convect with time due to the net induced velocity at its position produced by all the other vortices in the model. The velocities on each side of the splitter plate, $U_1 = 261.04\,\mathrm{m\,s^{-1}}$ and $U_2 = 34.7\,\mathrm{m\,s^{-1}}$, were chosen to match those of the AEDC shear layer. These yielded an initial circulation density, $\gamma_d = U_2 - U_1 = -226.34\ \mathrm{m\ s^{-1}}$, for the vortex sheet and an imposed convection speed

$$U_{cn} = (U_1 + U_2)/2 = 147.9\,\mathrm{m\,s^{-1}}. \tag{3.1}$$

The initial vortex core radius $\delta_i/2$ for the free vortices was varied to model different splitter-plate boundary-layer thicknesses; during this study, $\delta_i/2 = 8.626$, 17.25, and 34.5 mm. Holographic interferograms obtained during the AEDC experiments suggest the experimental splitter-plate boundary-layer thickness corresponded to the $\delta_i/2 = 8.626$ case (Havener & Heltsley 1994; Fitzgerald & Jumper 2002*a*). (No boundary layer measurements were performed in the AEDC facility (R. Cayse, personal communication 1998).) With an initial core diameter and a core growth rate function based on the growth rate of a laminar shear layer (Fitzgerald 2000), the (instantaneous) shear-layer discrete-vortex trajectories shown in figure 2 were produced.

The mean velocity profiles can be collapsed by suitably non-dimensionalizing the velocity (Schlichting 1979)

$$U^* = (U - U_2)/(U_1 - U_2) = [1 + \mathrm{erf}(y^*)]/2 \tag{3.2}$$

and the y-position (Samimy & Elliott 1990)

$$y^* = (y - y_{0.5})/\delta_\omega \tag{3.3}$$

where $y_{0.5}$ is the y-position where $U = U_{cn}$. Using this non-dimensionalization, the computed mean velocity profiles compare well with both incompressible and weakly compressible ($M_c = 0.51$) experimental measurements as shown in figure 3. DVM profiles are shown at several x-stations; the agreement increases with increasing x.

Similarly, the r.m.s. streamwise and lateral velocity fluctuations as well as the Reynolds stress can be compared to the corresponding experimental results as shown in figures 4 and 5. In figures 4 and 5, the peak DVM values increase with increasing x. Similarity of the DVM velocity fluctuation and Reynolds stress profiles would be expected to occur at larger x than required for mean velocity profiles (White 1991). The variation in profile magnitude and shape with x suggests that similarity conditions have not yet been reached for the δ_i shown. Even so, the DVM fluctuation profiles seem more likely to produce similarity profiles more like those measured in incompressible flows (i.e. like Wygnanski & Oster 1982) or the two-dimensional Euler simulation of Liou *et al.* (1995) than those measured by Samimy & Elliott (1990) in

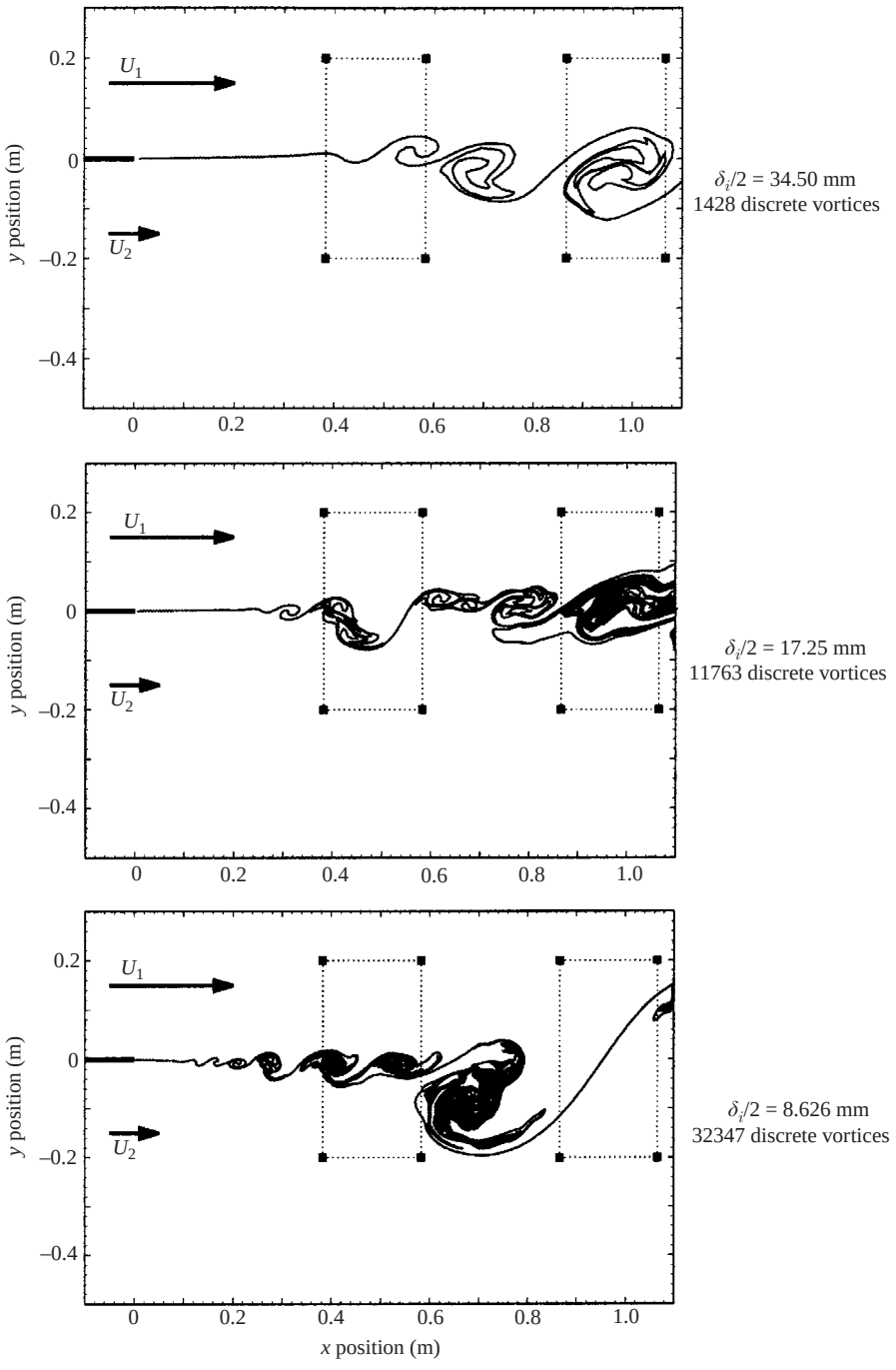

FIGURE 2. DVM shear-layer rollup variation with initial thickness $\delta_i/2$. Each curve is the locus of discrete vortex centres. Dotted boxes show positions of fields used in aero-optical computations (corresponding to observation stations 2 and 3 of the AEDC experiment).

a weakly compressible (but supersonic) shear layer. The disagreement between the DVM and the high-speed experimental results could be due to Mach-number effects not simulated in the incompressible DVM.

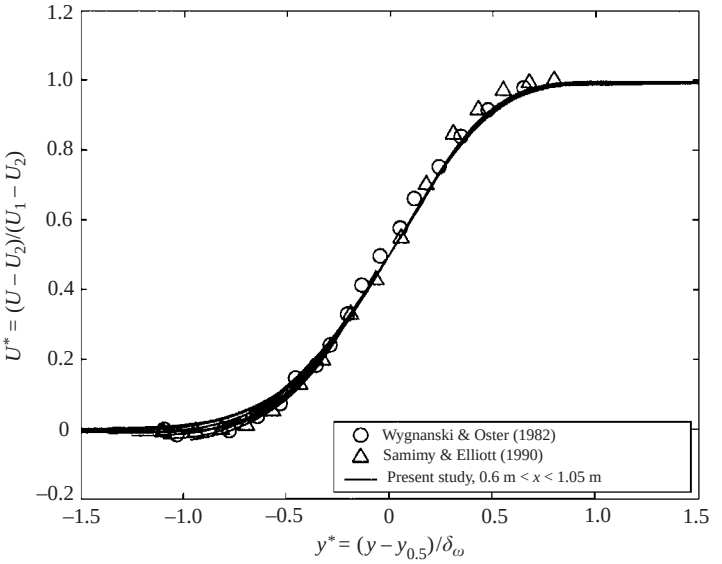

FIGURE 3. Comparison of DVM mean velocity profiles ($\delta_i/2 = 34.5$ mm) with experimental measurements in incompressible (Wygnanski & Oster 1982) and weakly compressible (Samimy & Elliott 1990) shear layers.

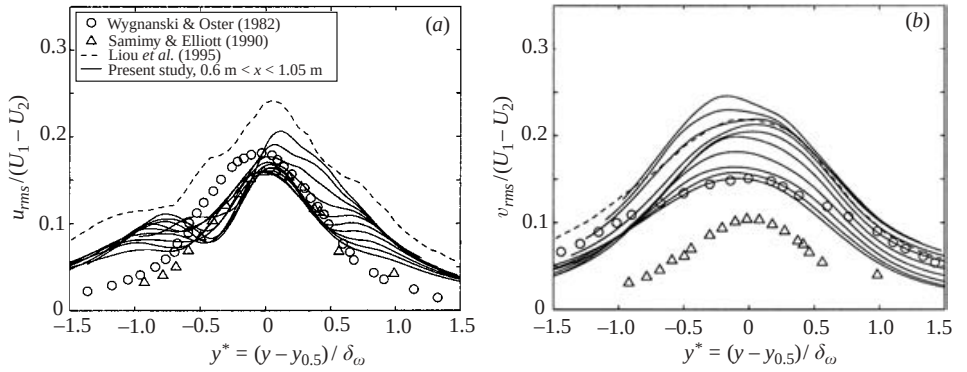

FIGURE 4. Comparison of DVM r.m.s. longitudinal (*a*) and lateral (*b*) velocity fluctuation profiles ($\delta_i/2 = 34.5$ mm) with experimental measurements in incompressible (Wygnanski & Oster 1982) and weakly compressible (Samimy & Elliott 1990) shear layers. The compressible-Euler numerical result of Liou *et al.* (1995) is also shown.

The shape of the DVM's longitudinal fluctuation profiles suggest this may be a Reynolds-number issue. Similarly shaped profiles were obtained by Ashurst (1979) in a DVM simulation and in the water tunnel experiments of Winant & Browand (1974) and of Browand & Weidman (1976). Indeed, the present DVM result agrees better with these latter data as shown in figure 6. The measurements of Winant & Browand (1974) showed, in fact, that the magnitude of the central peak increased with increasing x while the secondary peak (low-speed side 'shoulder', cf. figures 4 and 6) gradually disappeared, taking on a shape normally associated with fully turbulent shear layers (Winant & Browand 1974). Such a local maximum on the

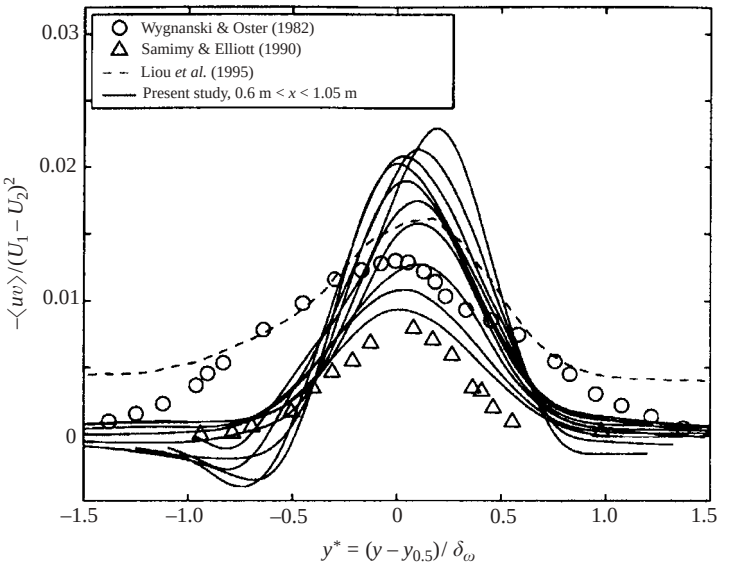

FIGURE 5. Comparison of DVM Reynolds stress profiles ($\delta_i/2 = 34.5$ mm) with experimental measurements in incompressible (Wygnanski & Oster 1982) and weakly compressible (Samimy & Elliott 1990) shear layers. The compressible-Euler numerical result of Liou *et al.* (1995) is also shown.

low-speed side of the layer is predicted by the linear stability theory of Michalke (1965) for spatially growing shear layers and suggests that the DVM behaves as if the splitter-plate boundary layers were laminar. This behaviour of the longitudinal velocity fluctuations may result because only eddies of size δ_i and larger are directly simulated. Thus the poor agreement between the DVM's turbulence profiles and the high-speed experiment could be a Reynolds-number effect. It could also be that the DVM better emulates the more truly two-dimensional shear layers that occur at much lower Reynolds numbers than that of the AEDC shear layer.

The growth of δ_ω with increasing x for the present numerical simulation is shown in figure 7. The shear-layer growth rate for all initial core sizes is the same. Once the shear layer's thickness, δ_ω, becomes large enough (versus vortex core size), the Kelvin–Helmholtz instability can be resolved and shear-layer rollup begins. Upstream of this point (for a given initial vortex core diameter), the instability cannot be spatially resolved so $\delta_\omega \approx \delta_i$. According to the empirical literature (Brown 1974), the shear-layer growth rate at the AEDC M_{c1} can be predicted using the relation

$$\delta/x = C_\delta \frac{(1-r_u)\left(1+s^{1/2}\right)}{1+r_u s^{1/2}}, \tag{3.4}$$

where $r_u = U_2/U_1$, $s = \rho_2/\rho_1$ and the constant $C_\delta = 0.085$ (Brown & Roshko 1974). For the conditions tested at AEDC ($r_u = 0.132$ and $s = 0.89$), (3.4) would predict a growth rate of 0.128. The growth rate realized for the DVM, $\Delta\delta_\omega/(x - x_0) = 0.139$ (with $x_0 = 0.06$ m and effectively $s = 1$) is within 8.6% of this predicted value. As such, the numerical simulation reasonably modelled the two-dimensional velocity field of a subsonic weakly compressible shear layer.

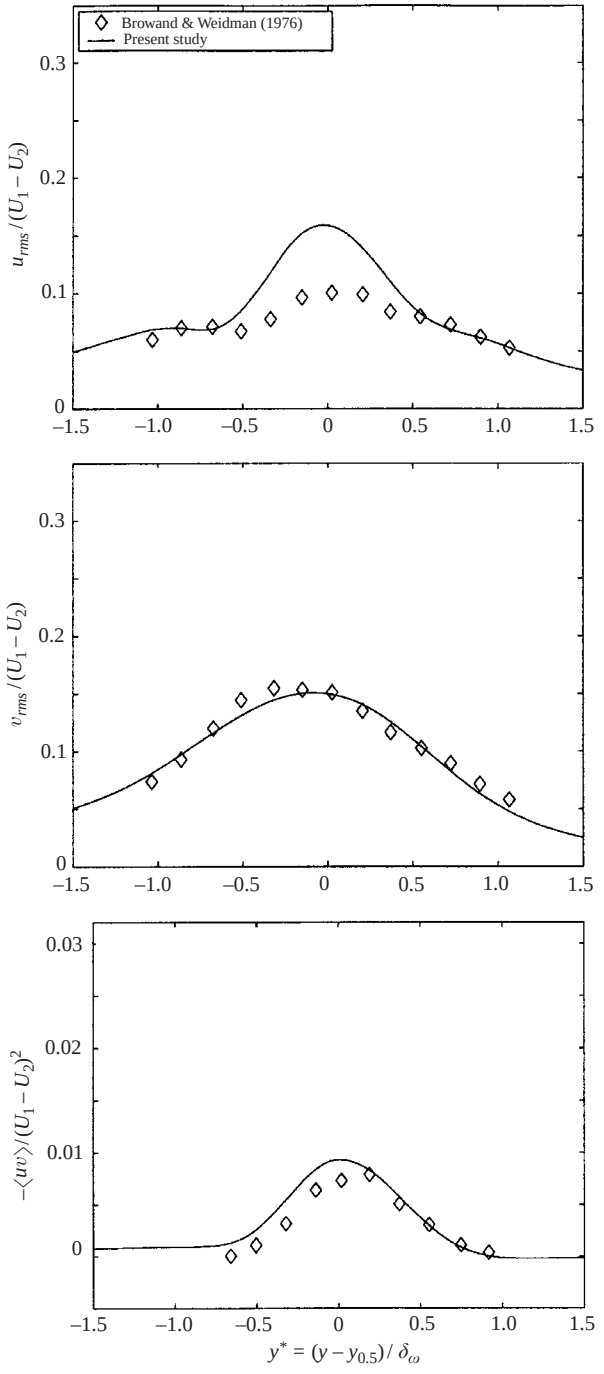

FIGURE 6. Comparison of DVM turbulence profiles ($\delta_i/2 = 34.5$ mm, $x = 0.6$ m) with experimental measurements in a water-tunnel shear layer by Browand & Weidman (1976).

4. Weakly compressible index model

The weakly compressible model developed during the present study was produced by first considering the 'conventional wisdom' first-order cause for the density (i.e.

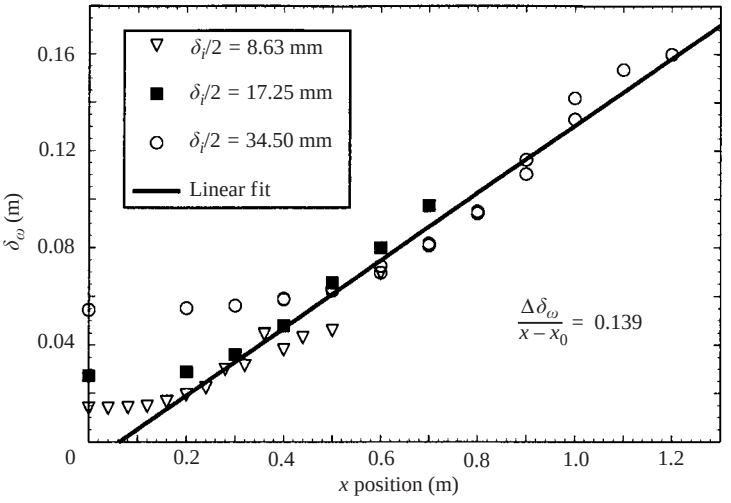

FIGURE 7. Growth of the discrete-vortex shear layer in terms of vorticity thickness.

index of refraction) variation, that being the static temperature difference between the low- and high-speed streams. When this mechanism failed to explain the measured AEDC wavefront data, a second (and ultimately a third) mechanism were added to model the next most-probable mechanisms. Since the optics calculation method was common to all stages of the model development process, this section begins by discussing the numerical optics procedure used for the weakly compressible cases, followed by the index-of-refraction modelling itself and resulting optical aberrations.

4.1. *Shear-layer optics*

For a matched-total-temperature shear layer of a single constituent fluid (like that tested at AEDC), all index-of-refraction field variations must be caused by the physics associated with the velocity field. The optical distortion calculations were, therefore, tied to the rectangular array of grid points at which a time series of instantaneous realizations of the velocity had been computed by the DVM. Using the index-of-refraction modelling described below, the instantaneous index field $n(t, x, y)$ was computed at each of the grid points. Optical aberrations (at each time step) were then computed by numerically evaluating (1.1) using the computed n field and a trapezoidal integration scheme. The total number of grid points was limited to ~ 2048 points to keep the index field's computational requirements reasonable (cf. § 4.3 below). The grid, therefore, had 32 streamwise points and 64 points in the beam-propagation (y-)direction. A (streamwise) aperture of 20 cm was chosen to permit good spatial resolution of the largest flow structures expected at AEDC stations 2 and 3 (cf. figure 2). This aperture was more than twice the AEDC experimental aero-optical window dimension, although 20 cm matches the diameter of the schlieren-path windows at each location shown in figure 1 (Havener & Heltsley 1994). Any index model based on the velocity field will continue to produce optical distortions well into the 'free-stream' regions of the flow because free-stream velocity differences computed by the DVM exist out to large $|y|$. Since, even at double-precision machine accuracies, long-pathlength integrations can accumulate errors to produce appreciable *OPD* error (Cassady, Birch & Terry 1989), the numerical beam was only propagated from $y_1 = -0.2$ m to $y_2 = 0.2$ m for the present study. For the present DVM,

integrating to 80 m was found to introduce machine and computational errors of $\sim 0.1\,\mu$m. By stopping the integration at $y_2 = 0.2$ m, it is estimated that an error of less than 0.008 μm has been introduced into the present OPD calculation. The integration path length chosen also corresponded to the approximate height of the AEDC test section at station 2 and ensured that approximate free-stream velocity conditions were reached, based on station 3 mean velocity profiles. The positions and overall size of the aero-optical grids are compared to the DVM shear layers in figure 2.

To make direct comparisons with the AEDC experimental data, the numerical wavefronts needed to be computed over the same (5 cm) aperture used in the measurements. For these 'reduced aperture' cases described in § 4.2 and § 5.1.2 below, only the portion of the full-aperture OPD result within the smaller aperture was retained. A new $\overline{OPL}$ was computed over this new aperture, and the resulting OPD was obtained using (1.2).

4.2. *Adiabatic-heating and cooling mechanism*

With a reasonable approximation to the weakly compressible two-dimensional shear-layer velocity field provided by the DVM and a scheme to determine the optical distortion found, the density changes (and concomitant index-of-refraction changes) which produce aero-optic distortions still need to be modelled. As mentioned above, the first layer of modelling (or 'mechanism') assumed that density differences resulted from static temperature variations in the flow produced by Mach number variations alone (Fitzgerald & Jumper 1998) as suggested by the experimental aero-optics practice of estimating OPDs from hot-wire data (Rose 1978; Rose, Johnson & Otten 1982; Rose & Johnson 1982). This model was based on the reasonable assumption of adiabatic flow since characteristic heat-transfer times due to local temperature gradients are long compared to convection times. Thus, for the AEDC conditions (common T_0), the higher-speed stream would enter the shear layer with a lower static temperature than the lower-speed stream. As the higher-Mach stream was slowed by the mixing process, it would increase in temperature. Conversely, the lower-Mach stream would decrease in temperature as it was accelerated by the higher-Mach stream.

The density, temperature, and pressure can be related through the ideal gas law and the energy equation (from the first law of thermodynamics). For unsteady adiabatic flow of a perfect gas with negligible body forces (and neglecting viscous terms), the energy equation is given by (Anderson 1990)

$$\frac{\mathrm{D}T_0}{\mathrm{D}t} = \frac{1}{\rho C_P}\frac{\partial p}{\partial t}, \tag{4.1}$$

where T_0 is the total temperature, C_P is the specific heat at constant pressure, and p is the static pressure.

To proceed further, some knowledge of the static pressure variation is required. One approach would be to assume isentropic expansion/compression. There are two difficulties with this approach. First, since a real turbulent shear layer is unstable, irreversible and has energy losses through viscous actions, it seems unreasonable to assume the flow is isentropic. Secondly, because the two streams are static-pressure matched but at very different initial velocities, a total pressure mismatch exists across the layer. Thus, at positions in the layer where the two streams would be in contact and at approximately the same local velocity (e.g. on either side of a 'braid' connecting two vortex rollers), isentropic relations would predict static pressure discontinuities

of tens of kPa (several psi). If such pressure discontinuities occurred in real flows, the shear-layer position would be deflected since the shear layer cannot support a cross-stream pressure gradient. No such deflection has been observed in the experimental literature (see e.g. Hall *et al.* 1993) Clearly, isentropic expansion/compression would be a poor assumption.

The assumption of negligible fluctuating static-pressure change ($p' \approx 0$) has long been used for compressible flat-plate boundary layers in non-hypersonic flows. This assumption was originally made out of convenience in order to extract velocity and static temperature data from hot-wire measurements of mass flux and total temperature in compressible boundary layers (Kistler 1959; Kovasnay 1950). Later, supersonic boundary layer measurements confirmed that for compressible boundary layers, p'/p is small (Kistler & Chen 1963; Gross, McKenzie & Logan 1987). Morkovin's strong Reynolds analogy (SRA) also leads to this result (Morkovin 1962; Lutz 1989; Smith & Smits 1993; Lele 1994; Smits & Dussauge 1996). Making the assumption that the static pressure across and through the shear layer is constant, (4.1) becomes

$$\mathrm{D}T_0/\mathrm{D}t = 0. \tag{4.2}$$

Equation (4.2) shows that for an inviscid flow with negligible pressure fluctuations, the total temperature of a 'turbule' of fluid would remain constant as it navigates whatever tortuous path it may in the shear-layer mixing process. Experimental evidence has shown, in fact, that T_0 fluctuations in non-hypersonic compressible boundary layers and wakes are also small (Kistler 1959; Demetriades 1968; Meier & Rotta 1971). It is interesting to note that if constant total temperature had been assumed instead, as is the assumption of Cebeci & Smith (1974) for a compressible turbulent boundary layer, based on experimental results of Kistler (1959), the consequence would have been that the static pressure remained constant through the shear layer as shown by (4.1).

Upon integration of (4.2), the following relationships for static temperature, T, in terms of the (constant) total temperature T_0, and local velocity, respectively, are

$$T = T_0 - \frac{|\boldsymbol{V}|^2}{2C_P} = T_0 + \frac{(1-\gamma)\,|\boldsymbol{V}|^2}{2\gamma R}, \tag{4.3}$$

where $C_P = R\gamma/(\gamma - 1)$ and the gas has been assumed to be piecewise calorically perfect. Equivalently, (4.3) can be written in terms of Mach number, $M = |\boldsymbol{V}|/(\gamma RT)^{1/2}$ as

$$T = T_0 / \left[1 + \frac{(\gamma - 1)}{2} M^2\right] \tag{4.4}$$

which is the definition of total temperature. Once the local static temperature is known, the local density may be found through the perfect gas law, since the static pressure through the shear layer has been assumed to be a constant. Finally, the local index of refraction can be determined using the Gladstone–Dale constant, K_{GD}, from (Goldstein 1983)

$$n = 1 + \rho K_{GD}. \tag{4.5}$$

By (4.3)/(4.4) and (4.5), this 'adiabatic heating/cooling' mechanism presumes that fluctuations in the velocity/Mach numbers in the shear layer will produce sufficiently high local temperature gradients that these alone could explain the *OPD* patterns Hugo *et al.* (1997) had measured at AEDC. At the beginning of this research,

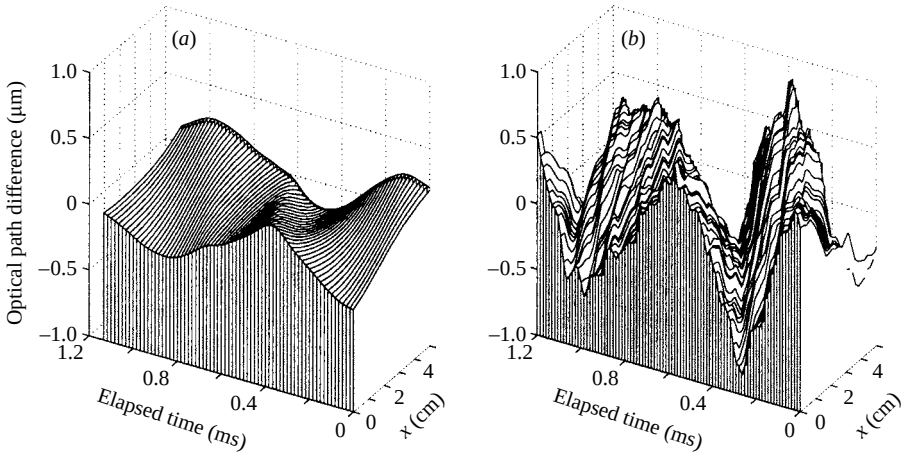

FIGURE 8. Comparison of wavefronts (*a*) computed using the 'adiabatic heating/cooling' index mechanism with (*b*) AEDC station 2 measurement as re-reduced by Fitzgerald & Jumper (2002*a*) using a 750 Hz high-pass filter.

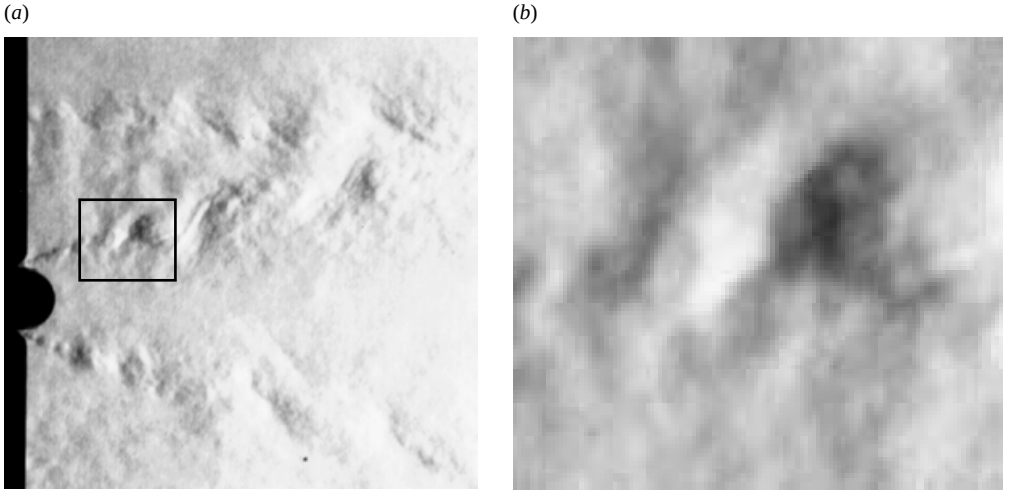

FIGURE 9. Experimental schlieren photograph of free shear layer shed from a cylinder in a $M = 0.6$ flow. Shear layer (*a*) and detail of two 'rollers' (*b*) marked by the rectangle in (*a*). (From Weston & Jumper 2002.)

this mechanism looked promising. The AEDC conditions would produce a 30°C temperature difference between the two streams with a corresponding fractional density difference, $\Delta\rho/\overline{\rho} = 0.12$. As shown in figure 8, the optical distortion resulting from this mechanism was fairly small and of the same order of magnitude as suggested by the model of Dimotakis *et al.* (2001); however, the measured AEDC optical distortions were almost an order of magnitude larger than either prediction (cf. table 1, § 5.1). In order to further assess this discrepancy albeit on a qualitative basis, simulated schlieren images were computed from the index-of-refraction field $n(t, x, y)$ using the method of Goldstein (1983). The resulting schlierens, while showing some hint of flow structure at high contrast, lacked the more detailed structure character of ubiquitously available schlieren images for this flow regime. An example of such an experimental schlieren is shown in figure 9 for a free shear layer produced

by Mach 0.6 flow separating off a bluff body (Weston 1982; Weston & Jumper 2002). This example was chosen because the fluids on both sides of the shear layer were known to be air at a matched T_0; the visibility of the structures in the schlieren has not been enhanced by mixing fluids of differing index of refraction. Such comparisons suggested that single-constituent shear flows can indeed produce optical distortions larger than those predicted by the adiabatic heating/cooling mechanism alone.

Since the adiabatic heating/cooling mechanism cannot produce *OPD* amplitudes of the same order as those measured at AEDC, then the SRA cannot be used for density predictions in subsonic nearly incompressible free shear layers. That the SRA breaks down for free shear layers has been suggested by several researchers (including Smits & Dussauge 1996; Lele 1994; Shyy & Krishnamurty 1997; Freund, Lele & Moin 2000); however, it continues to be extensively used when no practical alternative is available (see Smits & Dussauge 1996, for several examples). In fact, an SRA-type assumption is implicit in the scale sizes included in typical mixing-length- or eddy-viscosity-based turbulence models used in numerical computations; thus such models cannot predict the density variations produced by coherent structures (Cassady *et al.* 1989). Since adiabatic heating/cooling did not explain the experimental observations, other possible physical causes were examined.

4.3. *Mechanical-balance mechanism*

Even a casual examination of the velocity field in a frame moving with the convecting shear layer, as shown in figure 10 produced from the DVM, demonstrates an important contribution that has often been neglected by other researchers. Notice in figure 10 that the velocity field contains, not unexpectedly, considerable curvature. Similar streamline curvature is also evident in the velocity fields measured by Koochesfahani, Cohn & MacKinnon (2000) using laser-induced fluorescence (LIF) and molecular tagging velocimetry (MTV) and shown in figure 11. A simple analysis of a fluid in solid-body rotation (see Kuethe & Chow 1998, for example) yields an estimated concomitant pressure difference of approximately -14 kPa (-2 psi) for the AEDC conditions; clearly an assumption of negligible pressure fluctuations in this weakly compressible shear layer cannot be correct. Jones *et al.* (1979), for example, measured significant pressure fluctuations in a 0.45-Mach jet flow. The significance of pressure fluctuations in a separated shear layer or turbulent boundary layer was also apparent in other experimental (Cantwell & Coles 1983) and numerical studies (Sandham & Reynolds 1991; Leep *et al.* 1993; Chacín & Cantwell 2000; Freund *et al.* 2000). In fact, researchers using numerical turbulence simulations often choose pressure contours as a way of visualizing/identifying coherent turbulent structures (Sandham & Reynolds 1991; Leep *et al.* 1993; Chacín & Cantwell 2000; Freund *et al.* 2000).

A close approximation to the pressure distribution corresponding to a known (from the DVM) time-varying two-dimensional velocity field can be computed by integrating the unsteady Euler equations:

$$\frac{\partial p}{\partial x} = -\rho\left[\frac{\partial u}{\partial t} + u\frac{\partial u}{\partial x} + v\frac{\partial u}{\partial y}\right] \tag{4.6}$$

and

$$\frac{\partial p}{\partial y} = -\rho\left[\frac{\partial v}{\partial t} + u\frac{\partial v}{\partial x} + v\frac{\partial v}{\partial y}\right], \tag{4.7}$$

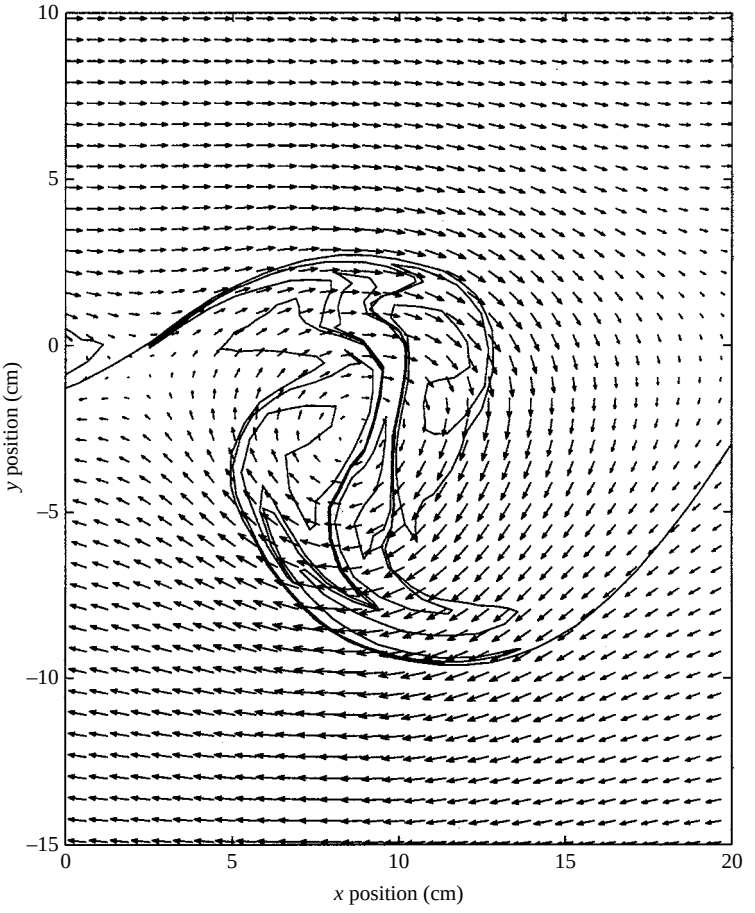

FIGURE 10. DVM velocity field as seen in a reference frame moving at convection velocity, $U_{cn} = (U_1 + U_2)/2$. Locus of DVM shear-layer discrete-vortex centres is also shown. (AEDC conditions, station 2 aperture, $\delta_i/2 = 17.25$ mm.)

because the viscous terms in the Navier–Stokes equations are four orders of magnitude smaller than the terms in (4.6) and (4.7). The partial derivatives on the right-hand sides of (4.6) and (4.7) were computed using a four-point central-difference scheme. Assuming (for the moment) that the density is known and independent of pressure, (4.6) and (4.7) yielded slopes to be integrated ($\partial p/\partial x$, $\partial p/\partial y$) at each point of a 32×64-point computational grid. The pressure field was then determined using the biquadratic spline formulation of Southwell (1980) to least-squares-fit a pressure 'surface' to the (4.6) and (4.7) slopes.

A first estimate of the (unknown) $\rho(t, x, y)$ in (4.6) and (4.7) was determined using the perfect gas law assuming $p_\infty = 0.6$ atm everywhere (the AEDC facility's free-stream pressure given by Havener & Heltsley 1994) with T given by the temperature field determined using only the adiabatic heating/cooling mechanism of § 4.2 (equation (4.3)). This provided an initial estimate of the $\rho(t, x, y)$ field, from which the new pressure field could be computed. In point of fact, the pressure surface thus computed provided a solution which is the zero-mean pressure fluctuation $p'(t, x, y)$ (i.e. satisfied the pressure gradient field but was not anchored to any mean pressure). The corrected-mean pressure was found by adding this $p'(t, x, y)$ to p_∞

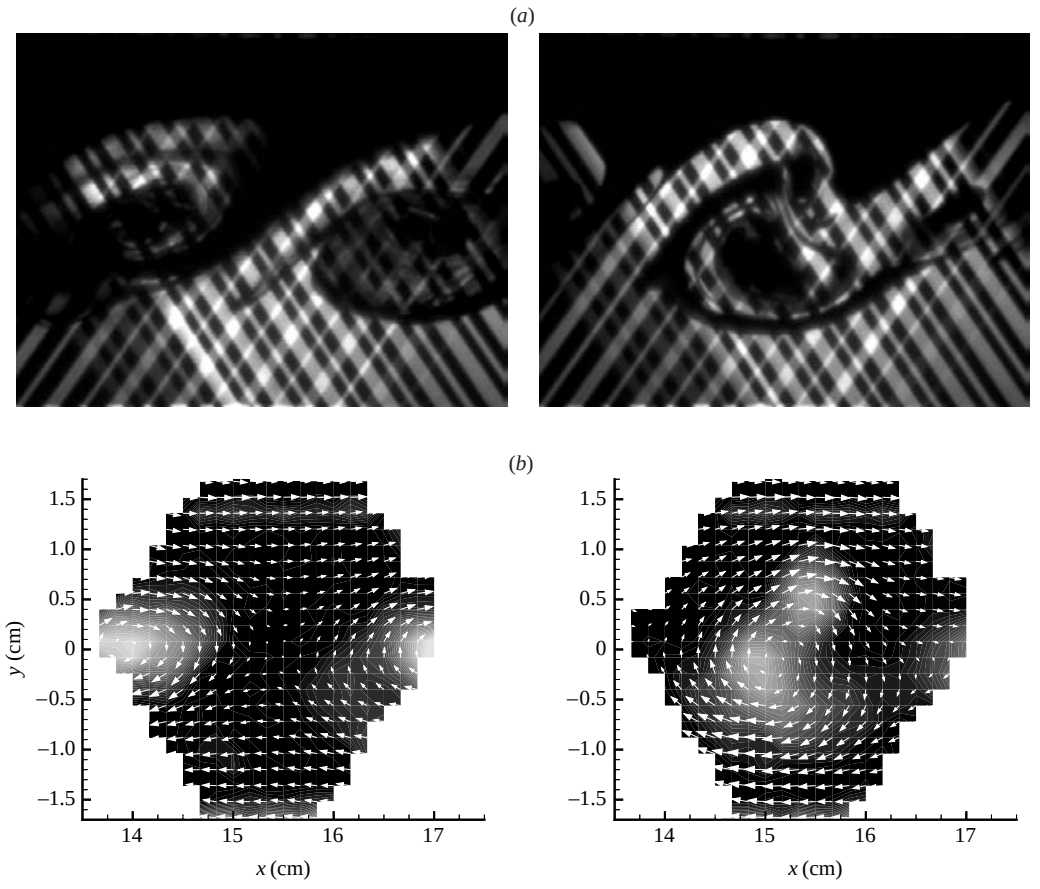

FIGURE 11. Two realizations of simultaneous velocity–concentration measurements in a turbulent two-stream shear layer. (*a*) LIF image (not processed), and (*b*) velocity/vorticity fields from MTV. Vorticity is shown in flooded contours and velocity field is in the shear-layer convection frame (from Koochesfahani *et al.* 2000).

(the non-zero constant of integration). With this new pressure field $p(t, x, y)$ and the original $T(t, x, y)$, a new $\rho(t, x, y)$ was computed. This iteration process was repeated until $\rho(t, x, y)$ converged, usually in less than 5 iterations.

Southwell's method had no way to impose the boundary conditions across the layer, namely, that $p = p_\infty$ at large $| y |$. These y-boundary conditions were imposed by removing any net $\partial p/\partial y$ at each x-station after the solution of $p(t, x, y)$ and before the new $\rho(t, x, y)$ was computed for the next iteration.

4.4. *'Rancque–Hilsch' mechanism*

Up to this point, it has been assumed that the total temperature $T_0(t, x, y) =$ constant in (4.3), as suggested by the initial adiabatic heating/cooling presumption. Recall from § 4.2 that the origin of (4.3) was the energy equation for an unsteady adiabatic flow with negligible body forces given by (4.1). In § 4.2, $\partial p/\partial t$ was assumed negligible as suggested in the literature; however, as was shown in § 4.3, $\partial p/\partial t$ cannot be zero. The effect of $\partial p/\partial t$ on the total temperature is clearly present in results computed as described in § 4.3.

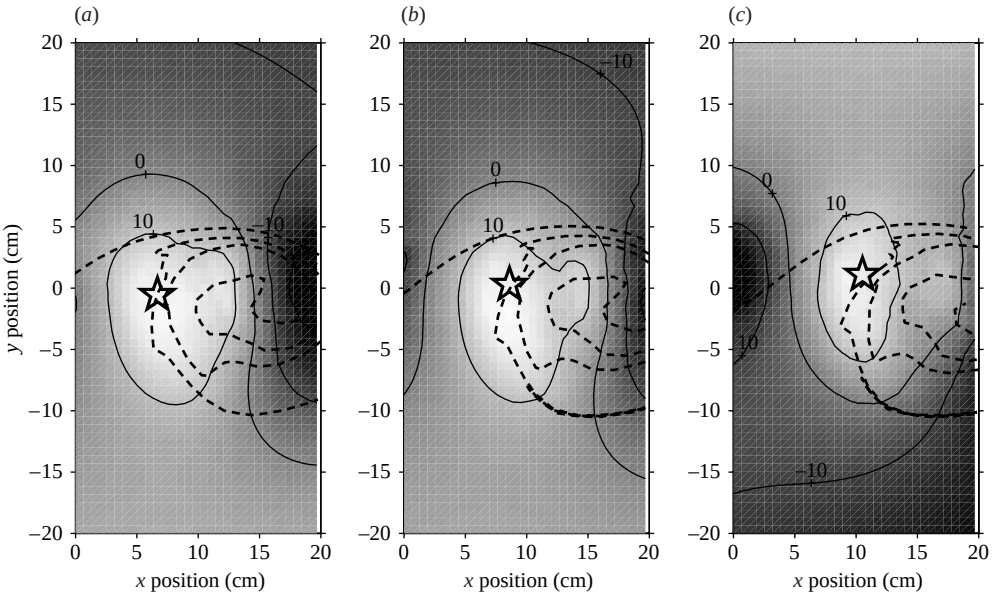

FIGURE 12. Gray-scale contours showing spatial variation of DT_0/Dt at three successive time steps (*a–c*). The star approximately marks the position of a fluid particle as it convects through the flow field. AEDC conditions, station 3 aperture, $\delta_i/2 = 35.6$ mm. Between frames, $\Delta t = 0.137$ ms; overall period = 0.274 ms. Dashed line marks locus of discrete-vortex centres, and contour values are in thousands of °C s^{-1}.

DT_0/Dt represents the change in T_0 that a 'turbule' of fluid would experience as it moves through the flow. Using the pressure field $p(t, x, y)$ computed as above, the DT_0/Dt field was computed for several time steps. This produced regions of positive and negative DT_0/Dt as shown in figure 12. The large star in figure 12(*a–c*) is moving at approximately the local flow velocity to mark the position of a 'turbule' of fluid at successive time steps. The fact that the 'star' starts and remains within a region of large positive DT_0/Dt (as a similar 'star' would remain within a region of large negative DT_0/Dt) suggests that the total temperature of individual fluid 'turbules' would change with time. Such changes in T_0 could produce 'hot' and 'cold' spots in the flow field where $|\Delta T_0|$ approached 100 °C (for 'turbules' that had travelled the length of the test section). (The contributions of the viscous terms neglected in (4.3) are three orders of magnitude smaller than $\partial p/\partial t$.) Such T_0 separations are reminiscent of those seen in a Ranque–Hilsch or 'vortex tube' (see e.g. Hilsch 1946; Kurosaka 1982). Analysis applied to such vortex tubes suggests a more correct method of computing the static temperature field to be used in the pressure/density iteration-loop solution of (4.6) and (4.7).

This total-temperature-separation effect was modelled by overlaying another iteration loop on the pressure/density iteration. After $\rho(t, x, y)$ had converged, the new loop modified the static temperature field $T(t, x, y)$ based on the isentropic relation (Anderson 1990; Hilsch 1946)

$$\frac{T(t, x, y)}{T_{ad}(t, x, y)} = \left[\frac{p(t, x, y)}{p_\infty}\right]^{(\gamma-1)/\gamma} \tag{4.8}$$

where $T_{ad}(t, x, y)$ was given by (4.3) with $T_0 = 27$ °C, as reported for the AEDC test (Havener & Heltsley 1994). A new $\rho(t, x, y)$ was then computed, and the

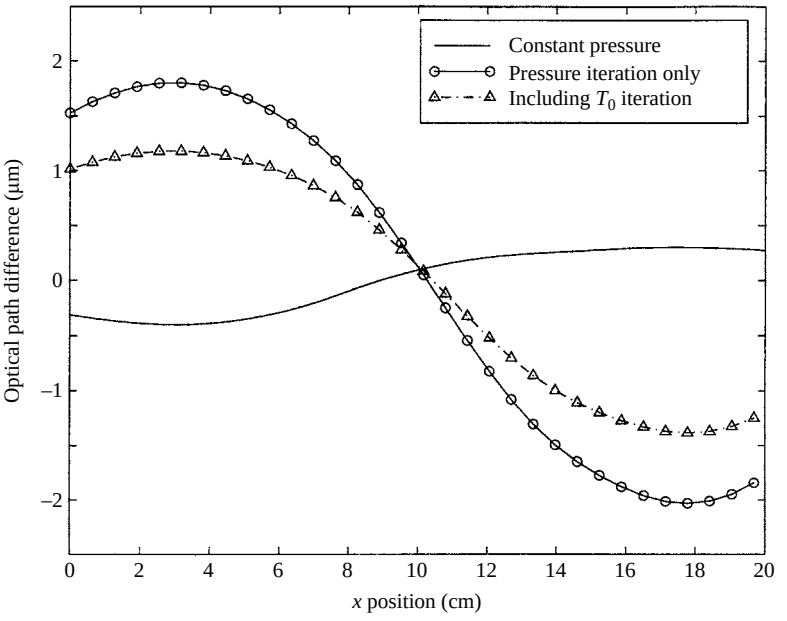

FIGURE 13. Effect of T_0 iteration loop on computed *OPD*. AEDC conditions, station 3 aperture ($x = 0.866$–1.066 m), $\delta_i/2 = 35.6$ mm, time step = 600.

density-iteration cycle was rerun. From the new converged pressure/density fields, $T(t, x, y)$ was recomputed using (4.8) and the process repeated until both temperature and density had converged at each time step. It should be noted that (4.8) produces the maximum theoretical change to the temperature field for a given pressure change (Hilsch 1946); the effect of (4.8) is to reduce the distortion amplitude due to the pressure/density iteration alone by as much as 35% as shown in figure 13. As was discussed in § 4.2, the flow is not expected to be isentropic. Thus, the actual *OPD* would be expected to lie somewhere between the two extremes represented by computations using the pressure/density iteration with and without the T_0 iteration. Figure 13 also shows how the addition of the mechanical pressure model changes *OPD* from the constant-static-pressure case considered in § 4.2. For the same velocity field, incorporating the pressure balance (both with and without the Rancque–Hilsch mechanism) significantly increases the amplitude while changing the sign of the distorted wavefront.

In that which follows, the full range of mechanisms discussed to this point (i.e. adiabatic heating/cooling, mechanical balance, and Rancque–Hilsch mechanisms) were adopted and will be referred to as the 'weakly compressible model'.

5. Weakly compressible simulation results

5.1. *Large-scale distortions*

The weakly compressible index-of-refraction model described in the previous sections produces index-of-refraction fields quite different from those typically seen when two incompressible fluids of different index (or different constituent fluids at high speed) are mixed. Such a 'two-index' flow typically has fairly distinct regions of mixed and unmixed flow where the mixed region has an index varying between the two unmixed values (Dimotakis *et al.* 2001). Figures 14 and 15 give a series of

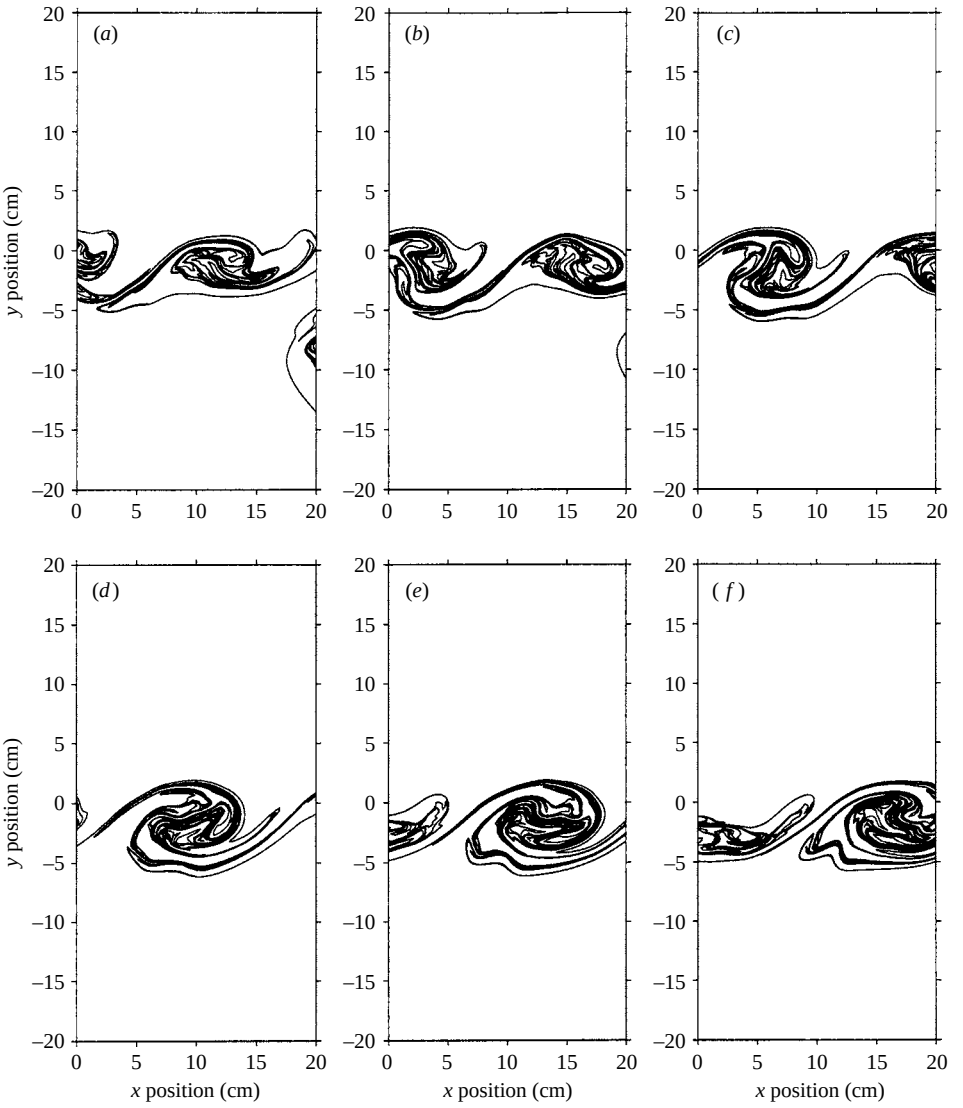

FIGURE 14. Locus of discrete-vortex centres showing DVM shear-layer evolution. AEDC conditions, station 2 aperture ($x = 0.383$–0.583 m), $\delta_i/2 = 8.625$ mm. Between frames, $\Delta t = 0.2167$ ms; overall period = 1.0833 ms.

discrete-vortex position maps, and the respective index-of-refraction fields that result from the weakly compressible model for a shear layer at the AEDC conditions. Unlike two-index cases, the model produces an index field that smoothly varies with the velocity field. As is clearly shown in figure 15, the weakly compressible model also expands the range of indices of refraction occurring in the flow field. The free-stream index values for the AEDC flow are $(n_1 - 1) \times 10^5 = 18.07$ and $(n_2 - 1) \times 10^5 = 16.08$ while $(n - 1) \times 10^5$ reaches 18.42 along vortex 'braids' and 14.67 in the centre of the 'rollers'. Thus, the weakly compressible model produces Δn of 3.7×10^{-5} while the Δn between the high- and low-speed streams is only 2×10^{-5}. Estimates based on the free-stream Δn would significantly underpredict the true optical distortion, as shown

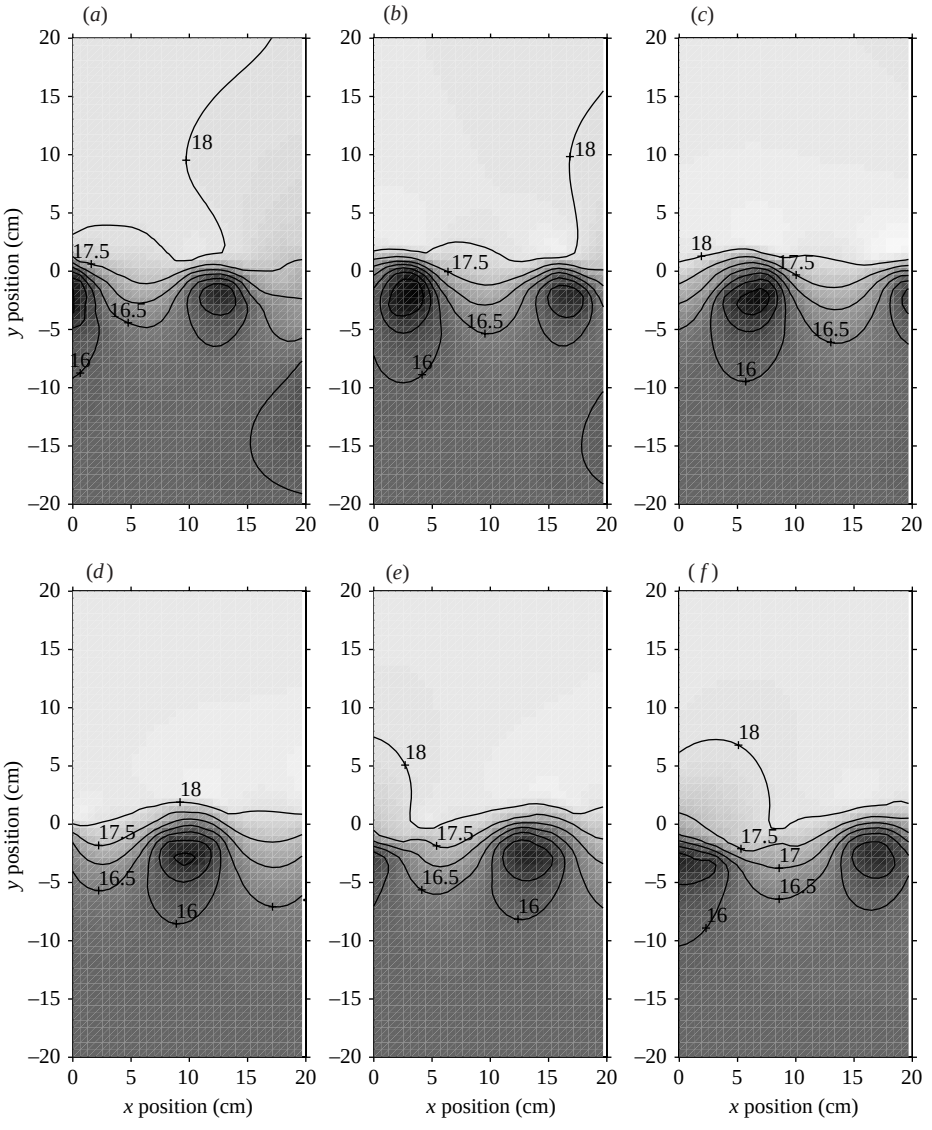

FIGURE 15. Weakly compressible model index-of-refraction fields shown as gray-scale contours. Contour values are $(n-1)\times 10^5$. AEDC conditions, station 2 aperture ($x = 0.383$–0.583 m), $\delta_i/2 = 8.625$ mm. Between frames, $\Delta t = 0.2167$ ms; overall period = 1.0833 ms.

in table 1. Since optical system performance drops exponentially with the square of *OPD* (Jumper & Fitzgerald 2001), these *OPD* underpredictions would translate into system performance overpredictions of two orders of magnitude or more, depending on the optical wavelength used by the system.

As alluded to in § 4.4, the instantaneous pressure distribution was the most significant factor in the resulting index (i.e. density) calculation. At a given time step, the static pressure varied by as much as 15 kPa throughout the field. A rough estimate of the r.m.s. pressure fluctuations at the centre of the shear layer, $p'_{\rm rms}/\overline{\rho}/{U_1}^2$, varied from 0.06 to 0.12 for the δ_i studied (the large variation can be attributed to an insufficient number of time steps for any δ_i to compute a true average). This is

	2-index mixing model	Dimotakis *et al.* (2001, § 5) model	Constant p (adiabatic ΔT) model	Weakly compressible model	AEDC experiment, station 2
$(n_{\max}-1)10^5$	18.0706	18.0706	18.9321	18.4314	–
$(n_{\min}-1)10^5$	16.0768	16.0768	16.0571	14.7629	–
$OPD_{\max}(\mu m)$	0.339	0.241	0.310	1.323	1.340

TABLE 1. Comparison of maximum and minimum indices of refraction and resulting *OPD*s computed using different n models together with AEDC experimental results. All models applied to the same DVM time step. (AEDC free-stream conditions: $M_1 = 0.8$, $M_2 = 0.1$, $n_1 = 1.0001807$, and $n_2 = 1.0001608$).

the same order as the 0.03 measured by Jones *et al.* (1979) for their slower $M = 0.45$ shear layer and as the 0.05 predicted by Freund *et al.* (2000) in their direct numerical simulation of an $M_{c1} = 0.41$ annular jet. More recent unsteady pressure measurements, specifically motivated by the present study, have also been made; in this case, the pressure signals were matched to the passage of coherent structures and showed time-resolved pressure fields of similar character and magnitude to those predicted by the weakly compressible model (Chouinard *et al.* 2002).

The weakly compressible model was successful in reproducing the gross features of schlierens like figure 9. Figure 16 illustrates the simulated schlieren images that result from these index fields (assuming a horizontal blade edge). Figures 14–16 correspond to AEDC station 2 and $\delta_i/2 = 8.625$ mm at the splitter plate. While no attempt has been made to match contour levels, a comparison of figure 16 with figure 9 shows that the full weakly compressible model produces distinct visible vortex structures in a schlieren, qualitatively like the shed vortices shown in the experimental image. In this sense, the model seems to capture the correct character of a nearly incompressible free-shear layer.

When *OPD*s are constructed from propagating an optical beam through the simulated n fields, wavefront aberrations corresponding to the shear layer's 'braids' and 'rollers' result. Figure 17 shows a time series of wavefronts generated by beam propagation through the time series of index fields (figure 15). A close comparison of figures 14–17 reveals that the valleys in figure 17 correspond to the vortex 'rollers' and the peaks to the 'braids'. The amplitude and streamwise wavelength of the distortions are proportional to the size of each individual 'roller' and change with the roller's temporal evolution. For the various cases examined during the present study, structure sizes of the *OPD*s varied from 6 to 20 cm, depending on the time window within the series, over the model's 20-cm aperture. This large aperture allows the large-scale *OPD* structures to be adequately defined.

5.1.1. *Initial shear-layer thickness effects*

An important result of the weakly compressible numerical simulation is the independence of the amplitude of the large-scale *OPD*s at a given aperture location (i.e. x-position) from the initial splitter-plate boundary-layer thickness (modelled in the DVM by $\delta_i/2$). This is strikingly shown by station 3 results. Figure 18 shows the discrete vortex maps for two different δ_i with the resulting pressure and index-of-refraction fields. The largest-scale structure in each case is of similar size and position (relative to the aperture). The resulting pressure and index fields are also quite similar; in these cases, the smaller vortex cores of the $\delta_i/2 = 17.54$ mm case allow

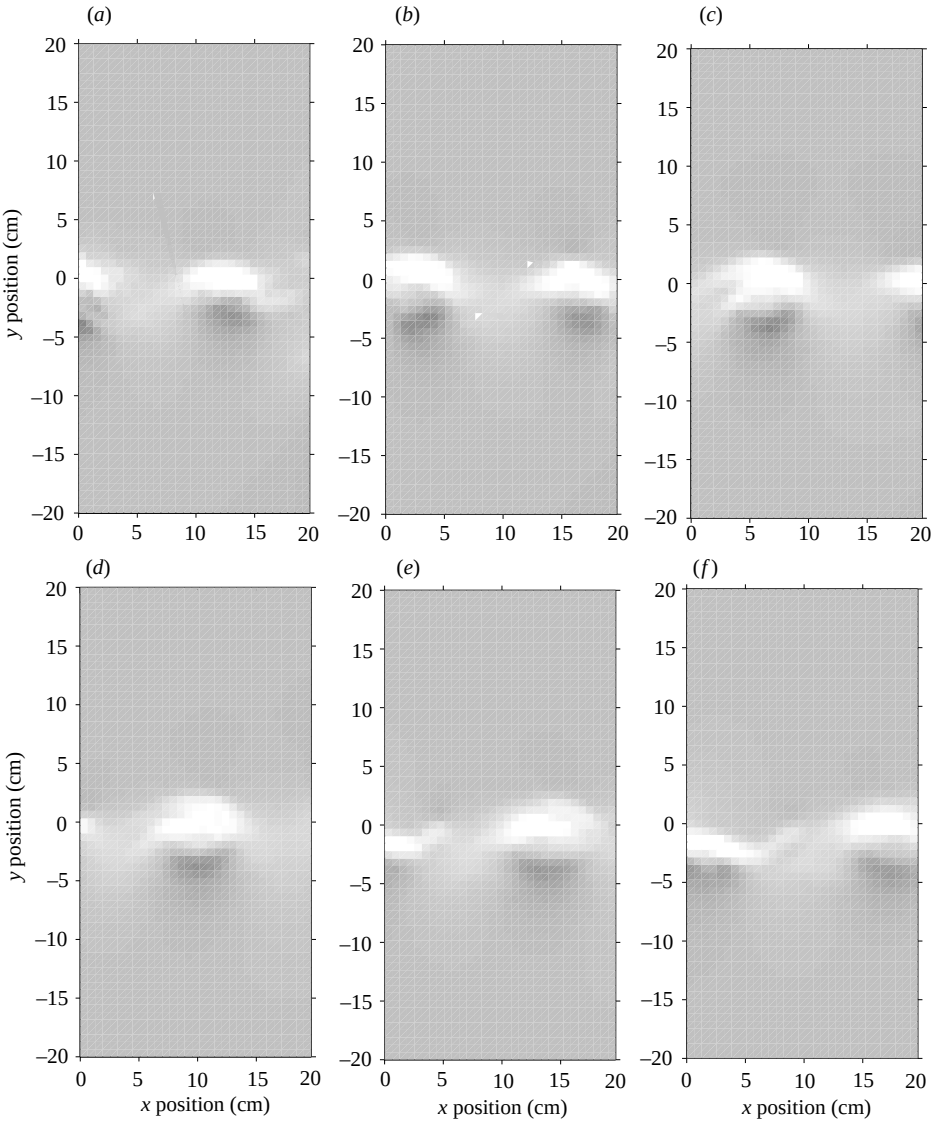

FIGURE 16. Simulated schlieren images of weakly compressible-model index-of-refraction field (horizontal knife edge). AEDC conditions, station 2 aperture ($x = 0.383$–0.583 m), $\delta_i/2 = 8.625$ mm. Between frames, $\Delta t = 0.2167$ ms; overall period $= 1.0833$ ms.

more detailed definition of the large-scale structure. It is not a surprise then that the resulting wavefronts in both cases match very closely as shown in figure 19. Thus at a sufficiently large x-location (i.e. following shear layer rollup and subsequent pairings) the largest-scale aero-optical effects are essentially independent of the initial splitter-plate boundary-layer thickness, assuming the initial thickness is small enough that rollup does occur. This has several practical implications for the aero-optics problem. First, if one is trying to simulate the shear layer, there is no significant increase in simulation fidelity using smaller vortex cores; therefore, larger core sizes can be used to reduce computational demands of the model. Similarly, other computational methods applied to aero-optical problems (such as large-eddy simulations) need only model the

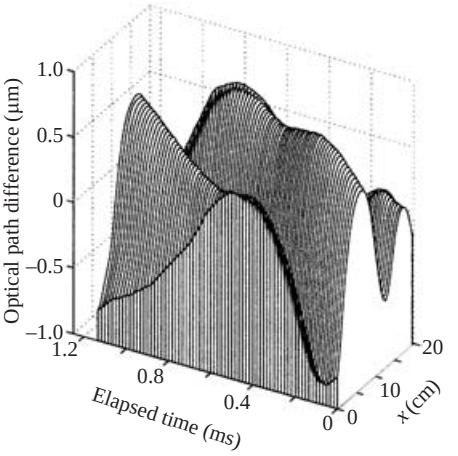

FIGURE 17. Optical wavefront distortions created by weakly compressible model, AEDC station 2, initial $\delta_i/2 = 8.625$ mm.

largest relevant flow structures. Secondly, it suggests two different potential distortion-mitigation strategies. Since large-scale structures produce the largest degradation on the far-field focusing of the beam (Cicchiello & Jumper 1997), one could try to thicken the splitter-plate boundary layers, thereby delaying the onset of the large-scale structures to beyond the aperture, albeit with a probable increase in small-scale distortions due to the large turbulent boundary layer feeding into the shear layer. Another strategy would be to use some sort of shear-layer control to regularize the vortex rollup, thereby making it amenable to some form of adaptive-optic correction (Gad-el-Hak & Blackwelder 1987; de Jonckheere *et al.* 1988). If the aperture was far enough downstream from the splitter-plate trailing edge, this latter option might be the only one available.

5.1.2. *Aperture effects*

As discussed in Fitzgerald & Jumper (2002*a*), the AEDC experimental test aperture would have served as a high-pass spatial filter with a 5-cm cut off because the test aperture was smaller than these structures. The effect of reducing the weakly compressible model *OPD* aperture to 5 cm is illustrated in figure 20. This figure used the same data as figure 17 except that the *OPD* was computed over a 5-cm aperture with the same centre as in figure 17. The large structures of figure 17 appear only as a large-amplitude time-varying tilt aberration. A large-scale tilt of similar frequency and amplitude was also seen in the AEDC measurements presented by Fitzgerald & Jumper (2002*a*) (after showing that the corner frequency of the high-pass vibration-removal filter discussed in Hugo *et al.* 1995, could be reduced from 2500 Hz to 750 Hz without corrupting the AEDC data) that were reproduced in figure 8. It is interesting to note that the best comparison between the model and experiment occurred for the DVM case using the smallest splitter-plate boundary layer feeding into the shear layer; that is, the case most closely approximating the experimental conditions. This best comparison is most likely happenstance only, however, attributable to a better match in shear-layer structure sizes, spacing, and (lack of) pairing within the aperture during the few milliseconds simulated. A comparison between the wavefronts predicted by the smaller two δ_i DVM cases for similar-sized flow structures (discussed in § 5.1.1) produced good agreement for both δ_i.

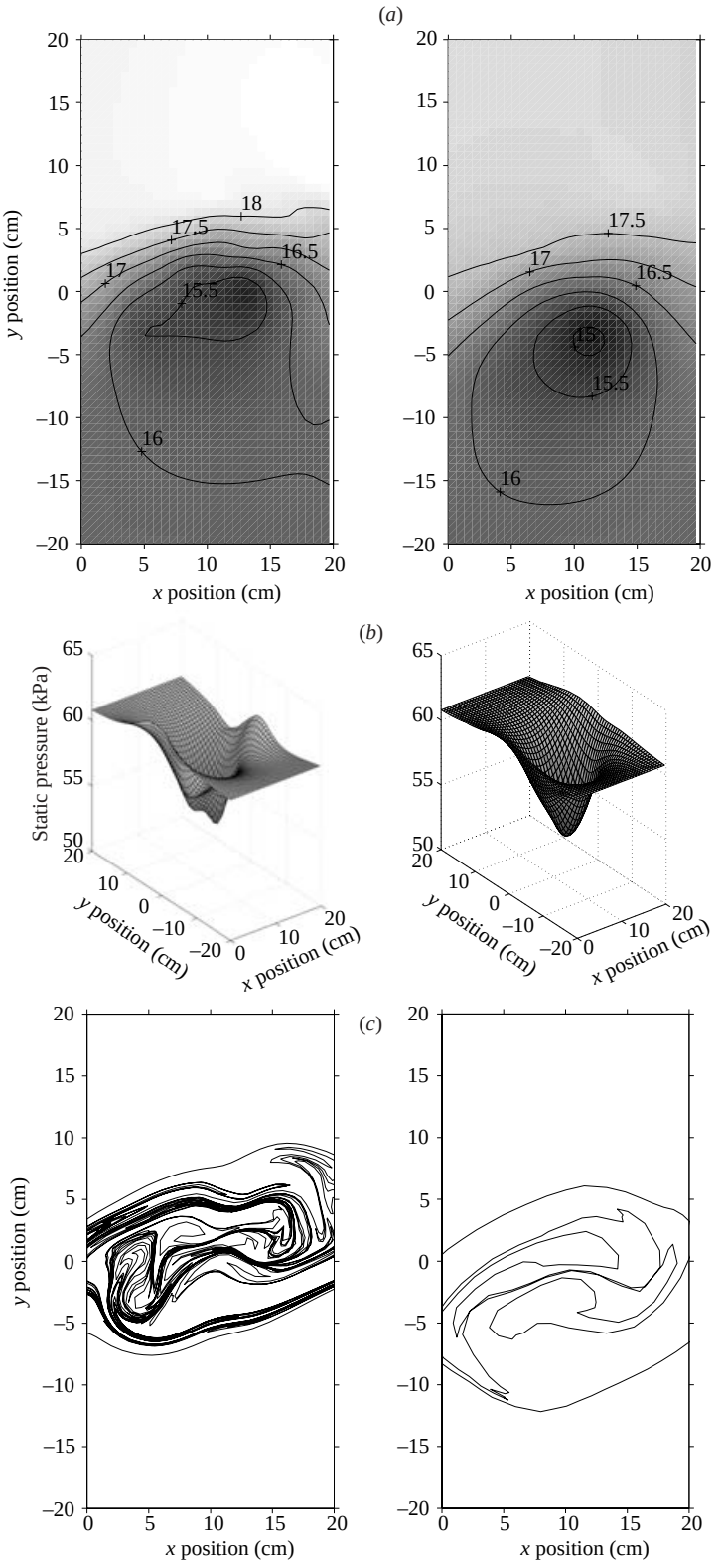

FIGURE 18. For caption see facing page.

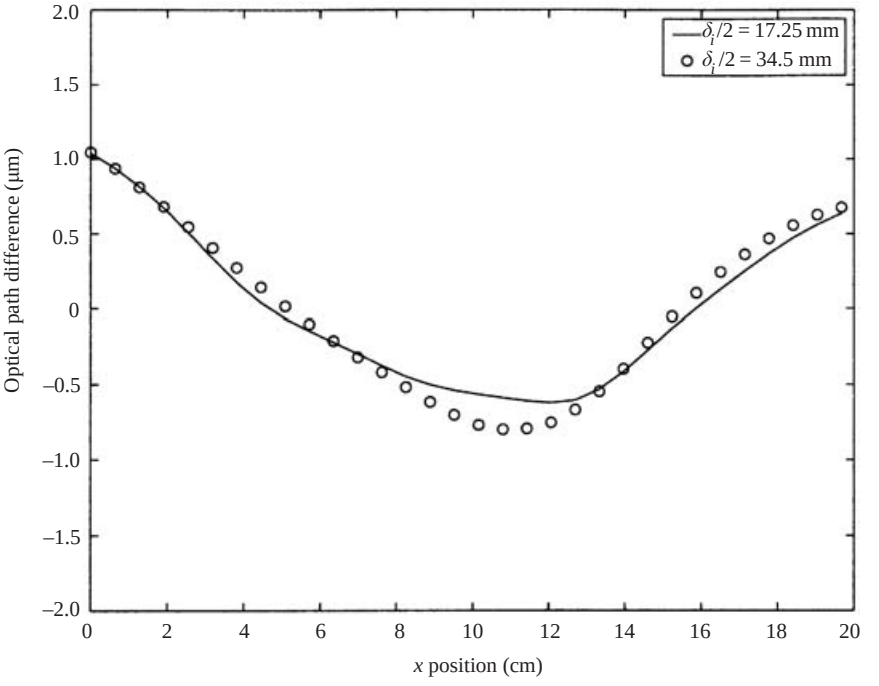

FIGURE 19. Comparison of wavefronts resulting from weakly compressible shear layer with different splitter-plate boundary-layer thicknesses (AEDC conditions, station 3 aperture).

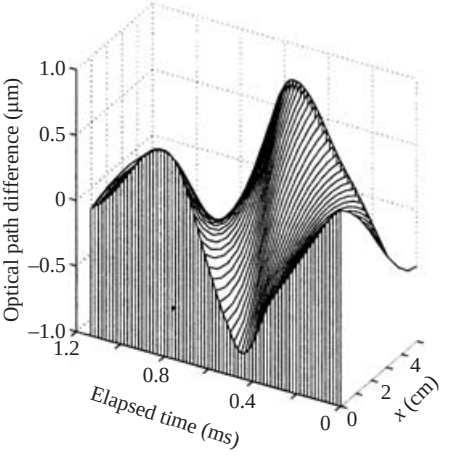

FIGURE 20. Figure 17 data (station 2, $\delta_i/2 = 8.625$ mm) recomputed over reduced (Hugo *et al.* 1997) aperture.

FIGURE 18. Weakly compressible-shear-layer simulation with two different splitter-plate boundary-layer thicknesses: $\delta_i/2 = 17.25$ mm (left) and $\delta_i/2 = 34.5$ mm (right) (AEDC conditions, station 3 aperture). (*a*) Index-of-refraction fields, (*b*) static-pressure fields, (*c*) locus of discrete-vortex positions.

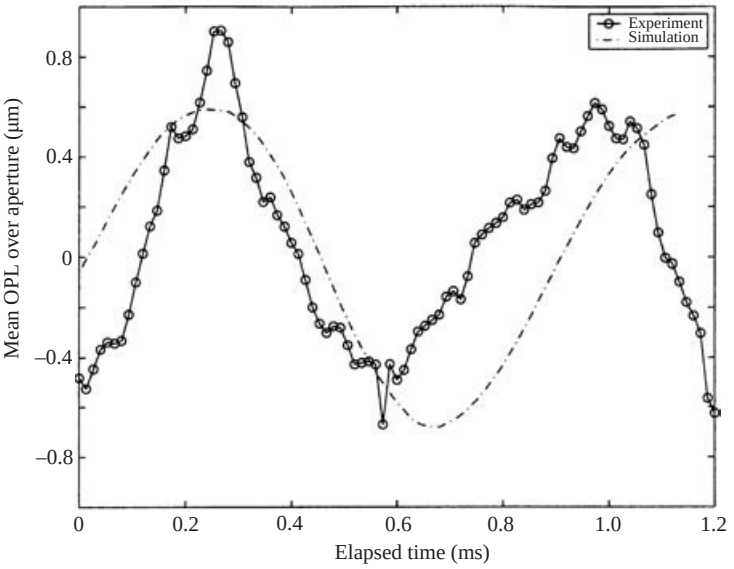

FIGURE 21. Variation of $\overline{OPL}$ removed in OPD calculation with time for experimental reconstruction (beam spacing = 2.54 cm, high-pass filter = 750 Hz) and weakly compressible model ($\delta_i/2 = 8.626$ mm), AEDC Station 2.

Another way of comparing the large-scale structures computed by the weakly compressible model and the AEDC data is by examining $\overline{OPL}(t)$. As discussed in Fitzgerald & Jumper (2002*a*), the average OPL over the aperture would be expected to change at a frequency corresponding to $\approx U_{cn}/\Lambda$ where Λ is a measure of the flow-structure size. A comparison of $\overline{OPL}(t)$ for the cases in figures 8 and 20 is shown in figure 21. The agreement in $\overline{OPL}(t)$ between the two cases is quite good. Figures 8 and 20 suggest that the weakly compressible model reasonably simulates the aero-optical distortion produced by the largest-scale flow structures. It should be noted that when these larger structures are considered (as would be necessary for apertures like the 20-cm aperture of figure 17), the OPD peak-to-peak aberration over the large aperture would be considerably larger than the approximately 0.8 waves originally reported by Hugo *et al.* (1997) (for wavefronts with the largest-scale structures filtered out).

5.2. *Small-scale distortions*

The major difference in the character of figures 20 and 8 is that the jagged character of the AEDC experimental data is not present in figure 20. The absence of finer-scale structure on the wavefronts in figure 20 was not initially an intuitive result. Figure 14(*d*), for example, shows a single instant in time for the shear-layer rollup; the tight wrapping of the curve is indicative of many vortex pairings. When mixing two incompressible fluids of differing index of refraction (i.e. two-index mixing), these complicated patterns of the dissimilar-index mixing produce sharp changes in the OPD. In the weakly compressible-shear-layer simulations, it was originally expected that pairing would mix multiple high-curvature swirling pockets within a larger swirling flow field. This would lead to multiple (relative) low-pressure regions. In fact, this mixing of the vortices produced a smooth swirling velocity pattern that gave an appearance more like one larger vortex (figure 10), thus producing a relatively smooth but deeper static pressure well as shown in figure 22. Such a smoothly varying

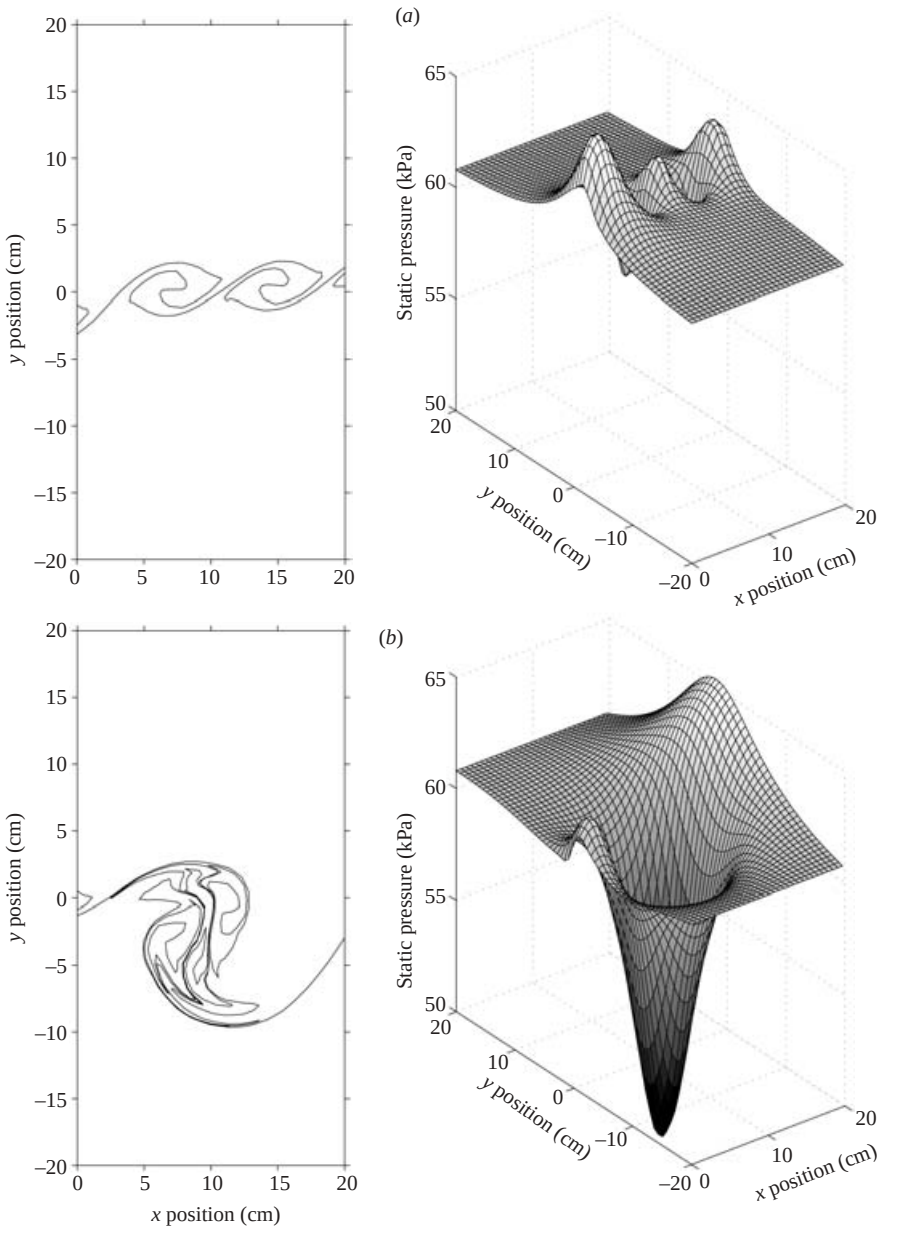

FIGURE 22. Instantaneous loci of discrete-vortex positions and static-pressure fields computed from DVM velocity fields. AEDC conditions, station 2 aperture, $\delta_i/2 = 17.25$ mm. (*a*) Prior to pairing and (*b*) following multiple pairings.

velocity pattern is also shown in the velocity fields measured by Koochesfahani *et al.* (2000) using LIF/MTV (figure 11). While averaging of tag velocities in the vicinity of each grid point is inherent in the MTV method, the pairing vortices in the second column of figure 11 produce a single swirling velocity region much like that of the DVM (cf. figure 10).

This lack of appreciable smaller-scale structure does not appear to be an artifact of insufficient velocity-field grid resolution. To investigate the effect of grid spacing

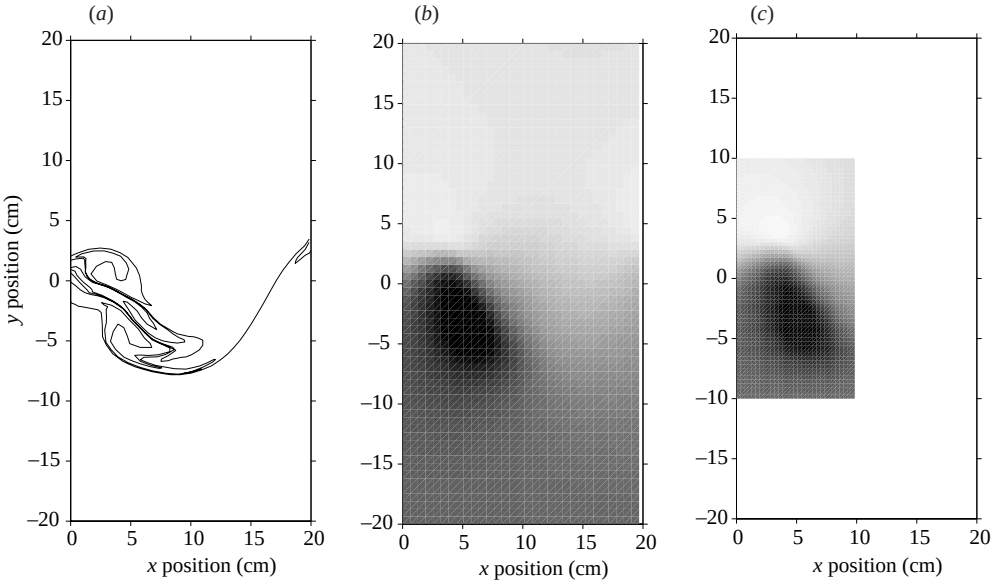

FIGURE 23. Effect of grid spacing on index-of-refraction fields. Index fields shown as gray-scale contours (labels removed for clarity). AEDC conditions, station 2 aperture, $\delta_i/2 = 17.25$ mm. (*a*) Locus of discrete-vortex positions, (*b*) standard grid, (*c*) reduced grid spacing.

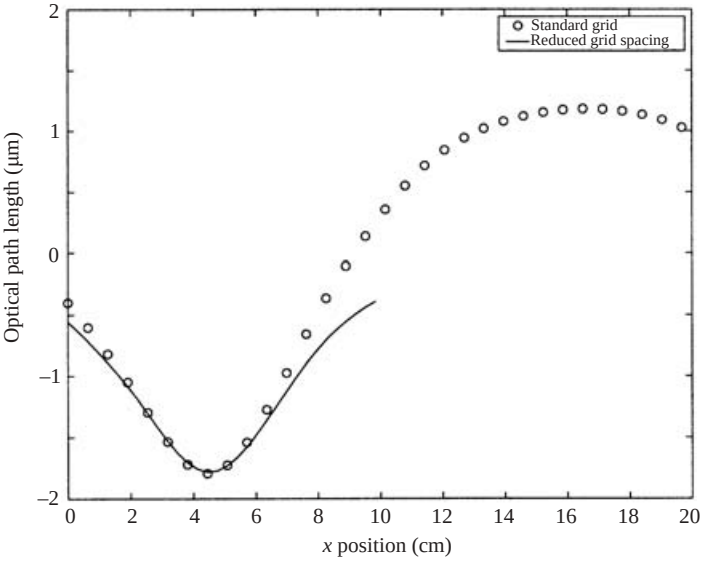

FIGURE 24. Effect of grid resolution on wavefront.

(*h*), a test case (using DVM results for $\delta_i/2 = 17.25$ mm) was recomputed with a new grid spacing of $h/2$. The resulting index fields for both grid spacings are compared in figure 23. The increased resolution does improve the index field definition but does not appreciably change the result. There is also little appreciable change in the corresponding wavefront, as shown in figure 24. The increased wavefront resolution reveals no additional small scales. This is ultimately due to the smoothly varying

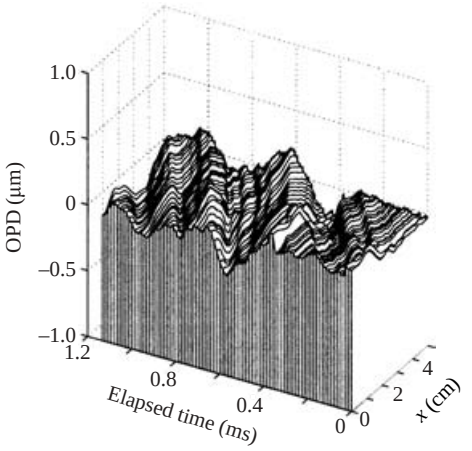

FIGURE 25. AEDC station 1 experimental wavefront reconstruction: beam separation $\delta = 2.54$ cm. High-pass filter: 750 Hz.

velocity field that was illustrated in figure 10. The only disagreement between the two wavefront results is at either end of the reduced grid's smaller aperture; the divergence between the two results in this case is an artifact caused by the insufficient x-dimension to resolve the pressure influences of the flow structures just outside the aperture.

Given that the weakly compressible numerical model reasonably simulates the large-scale distortions, it is left to understand the source of the small-scale distortions apparent in the AEDC wavefronts of figure 8. There are at least two potential contributors to the discrepancy. The first is that the DVM may not have adequately simulated the high Reynolds number of the AEDC flow. The DVM directly simulated two-dimensional vortices of diameter δ_i and larger while indirectly simulating those at the smallest scales (through growth of the vortex cores). Moreover, the DVM could not simulate three-dimensional shear-layer flow structures. At the AEDC Reynolds numbers, turbulence scales that are a fraction of δ_i and/or are created by three-dimensional flow structures (e.g. streamwise vortices in the 'braids' between 'rollers') could also be important. A simple solid-body-rotation vortex model would suggest, however, that an unrealistically high velocity difference would be required across a single small-diameter vortex to produce the 0.15-μm-amplitude aberration of spatial scale 1–2 cm that is typical in the AEDC experimental data. Due to the small longitudinal extent of these distortions, it would probably take a combination of several small flow structures (e.g. vortices) crossing the same optical ray at a single instant. In addition, fairly large velocity differences are required across each such vortex (~ 150 m s^{-1}) in order to produce the measured distortion amplitudes. Without such high velocity differences, the smaller-δ_i vortices would produce more subtle changes to the wavefront curvature (cf. figure 19) as opposed to distinct smaller-scale wavefront structures. Since OPD is an integral quantity, the number and size(s) of contributing flow structures cannot be deduced from the wavefront alone.

A second contributing explanation for the small-scale structures could be unintended flow 'contamination' of the optical signal by the test apparatus. Such a cause for the small-scale wavefront structures is suggested in the wavefront data measured over the 5-cm aperture starting 3.575 cm downstream of the trailing edge of the splitter plate (AEDC station 1 aperture). Figure 25 is a typical time series of

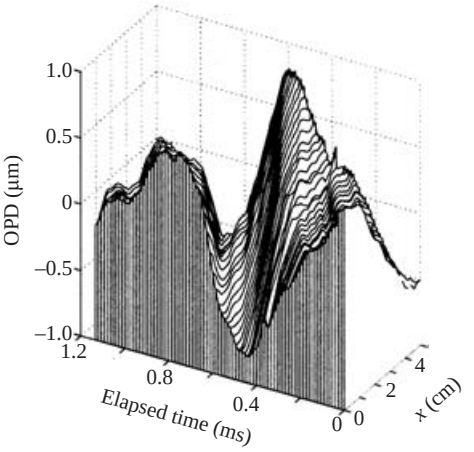

FIGURE 26. AEDC station 2 wavefronts produced by superposition of weakly compressible model results (figure 20) and station 1 experimental data (figure 25).

wavefronts measured at this location. Since shear-layer rollup may be ruled out at the beginning of the station 1 test aperture, and the structures are convecting at a velocity consistent with the shear-layer convection velocity, one explanation is that variant-density-flow structures produced by the boundary layer on the splitter plate were fed into the shear layer (see Fitzgerald & Jumper 2002*a*, for a full discussion). An additional and more likely source of small-scale distortions would be the turbulent boundary layer on the window in the high-speed wall of the test section. Both the splitter-plate and high-speed-wall boundary-layer thicknesses are of the same spatial order as the small-scale wavefront structures; moreover, a solid-body-rotation vortex model suggests that the velocity difference across the boundary layer is high enough to generate the small-spatial-scale distortions found at both stations 1 and 2. In either contamination scenario, distortions similar to those in figure 25 would be superimposed on the large-scale distortion.

To investigate these possible distortion mechanisms, the aberrations shown in figure 25 were linearly superimposed on the numerical results of figure 20 to produce figure 26. The simulated wavefronts in figure 26 have similar structure wavelengths to the experimental wavefronts of figure 8 as shown in figure 27. While the simulated structure amplitudes admittedly appear smaller than those in the corresponding experiment, it is clear that variant-density flow structures that had been entrained into the larger-scale swirling eddies of the shear layer and/or due to the turbulent boundary layer on the tunnel window would contribute to production of small-scale distortions. The fact that the small-spatial-scale distortions at the station 2 position suggest a growth in amplitude from the station 1 measurement is more consistent with wavefront contamination by passage through the turbulent boundary layer over the tunnel window on the high-speed side. This suggestion is further strengthened by a recent detailed study by Gordeyev *et al.* (2003) of the aberrating character of attached turbulent boundary layers at Mach numbers ranging through those of the AEDC test. Gordeyev *et al.* (2003) found that high-spatial-frequency turbulent-boundary-layer-flow structures produced *OPD*s with amplitudes and spatial scales consistent with the AEDC data.

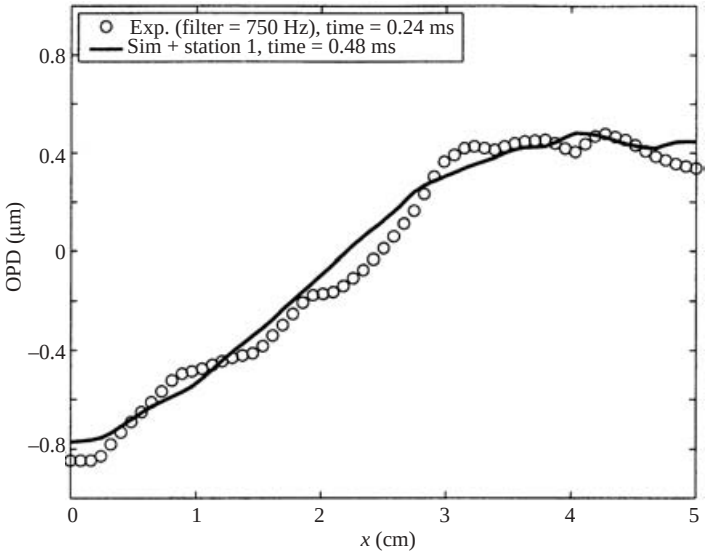

FIGURE 27. Comparison of individual AEDC station 2 experimental wavefront (from figure 8) with numerical simulation and superimposed station 1 wavefront (from figure 26) at corresponding time step.

6. Conclusions

The near incompressibility of a shear-layer flow field like that of the AEDC experiment suggested that the velocity field could be reasonably modelled by a two-dimensional discrete vortex model. Since the velocity field was known from the DVM, the instantaneous static pressure, temperature, and density fields could be obtained from the unsteady Euler equations (and an isentropic expansion correction) using a double iteration scheme. The resulting index field gave rise to simulated schlieren photographs similar to those ubiquitously reported in the experimental literature. Contrary to the authors' original expectations (Fitzgerald & Jumper 1998), pressure fluctuations associated with streamline curvature were a dominant influence on the instantaneous density field, producing index-of-refraction variations larger than the difference in free stream indices. Estimation techniques using only free stream Δn would thus significantly underpredict the distortion produced by the shear layer in the present study as shown in table 1.

The wavefronts generated by the numerical simulation appear to capture the large-scale aero-optical distortions measured by Hugo *et al.* (1995, 1997) at AEDC. The simulation could not, however, account directly for the small-scale distortions noted in the experimental results. The lack of small-scale distortions may be due to limitations in the modelling of three-dimensional and/or Reynolds-number effects. In addition, AEDC station 1 experimental wavefront data suggest that the compressible turbulent boundary layer on the optical access window in the tunnel wall contributes to these small-scale structures. Other contributors to these distortions may include variant-density flow structures fed into the shear layer from the splitter-plate boundary layer (see Fitzgerald & Jumper 2002*a*). Given an estimate of the small-scale-structure amplitude and wavelength, a first-order simulation of the data can be made by superimposing such distortions onto the large-scale distortion predicted using the numerical model.

The success of the numerical model in matching the AEDC measurements suggests the dominant distortion mechanism in a very weakly compressible shear layer to be the pressure change accompanying the layer's rollup (i.e. the organized two-dimensional coherent structures in the layer). If dedicated experiments can confirm these results, it follows that the dominant spatial frequencies of the aberrations may be lower than suggested by previously published AEDC data.

These efforts were sponsored by the Air Force Office of Scientific Research, Air Force Material Command, USAF, under Grant Numbers F49620-97-1-0489 and F49620-00-1-0025. The US Government is authorized to reproduce and distribute reprints for Governmental purposes notwithstanding any copyright notation thereon. The authors would also like to thank B. Cantwell and D. Papamoschou for their suggestions during this study.

REFERENCES

Anderson, Jr., J. D. 1990 *Modern Compressible Flow*, 2nd edn. McGraw-Hill.

Ashurst, W. T. 1979 Numerical simulation of turbulent mixing layers via vortex dynamics. In *Turbulent Shear Flows I* (ed. F. Durst *et al.*), pp. 402–413. Springer.

Beale, J. T. & Majda, A. 1985 High order accurate vortex methods with explicit velocity kernels. *J. Comput. Phys.* **58**, 188–208.

Brooke, M. A., Glezer, A., Jokerst, N. M. & Pearlstein, A. J. 1996 Neural network determination of optical phase correction in a plane shear layer using parallel optoelectronic image processing and global optical flow diagnostics. *Proc. AFOSR Image Reconstruction and Aero-Optic Metrology in Turbulence Workshop.* Air Force Office of Scientific Research, Westin Peachtree Plaza Hotel, Atlanta, GA.

Browand, F. K. & Weidman, P. D. 1976 Large scales in the developing mixing-layer. *J. Fluid Mech.* **76**, 127–144.

Brown, G. L. 1974 The entrainment and large structure in turbulent mixing layers. In *Fifth Australian Conf. on Hydraulics and Fluid Mechanics, Christchurch, New Zealand*, pp. 352–359.

Brown, G. L. & Roshko, A. 1974 On density effects and large structure in turbulent mixing layers. *J. Fluid Mech.* **64**, 775–816.

Cantwell, B. & Coles, D. 1983 An experimental study of entrainment and transport in the turbulent near wake of a circular cylinder. *J. Fluid Mech.* **136**, 321–374.

Cassady, P. E., Birch, S. F. & Terry, P. J. 1989 Aero-optical analysis of compressible flow over an open cavity. *AIAA J.* **27**, 758–762.

Cebeci, T. & Smith, A. M. O. 1974 *Analysis of Turbulent Boundary Layers*. Academic.

Chacín, J. M. & Cantwell, B. J. 2000 Dynamics of a low Reynolds number turbulent boundary layer. *J. Fluid Mech.* **404**, 87–115.

Chew, L. & Christiansen, W. 1991 Coherent structure effects on the optical performance of plane shear layers. *AIAA J.* **29**, 76–80.

Chew, L. & Christiansen, W. 1993 Experimental investigation of transitional free shear layer optics. *AIAA J.* **31**, 2290–2295.

Chorin, A. J. & Bernard, P. S. 1973 Discretization of a vortex sheet, with an example of roll-up. *J. Comput. Phys.* **13**, 423–429.

Chouinard, M., Asghar, A., Kirk, J. F., Siegenthaler, J. P. & Jumper, E. J. 2002 An experimental verification of the weakly-compressible model. *AIAA Paper* 2002-0352.

Cicchiello, J. M. & Jumper, E. J. 1997 Far-field optical degradation due to near-field transmission through a turbulent heated jet. *Appl. Optics* **36**, 6441–6452.

Demetriades, A. 1968 Turbulence measurements in an axisymmetric compressible wake. *Phys. Fluids* **11**, 1841–1852.

Dimotakis, P. E., Catrakis, H. J. & Fourguette, D. C. 2001 Flow structure and optical beam propagation in high-Reynolds-number gas-phase shear layers and jets. *J. Fluid Mech.* **433**, 105–134.

Fitzgerald, E. J. 2000 The shear layer compressibility mechanism and its role in creating aero-optical distortions. PhD thesis, University of Notre Dame, Notre Dame, Indiana.

Fitzgerald, E. J. & Jumper, E. J. 1998 Shear layer optical distortions due to compressibility vs. passive scalars. *AIAA Paper* 98-2834.

Fitzgerald, E. J. & Jumper, E. J. 2002*a* Aperture effects on the aerooptical distortions produced by a compressible shear layer. *AIAA J.* **40**, 267–275.

Fitzgerald, E. J. & Jumper, E. J. 2002*b* Scaling aerooptic aberrations produced by high-subsonic-Mach shear layers. *AIAA J.* **40**, 1373–1381.

Freund, J. B., Lele, S. K. & Moin, P. 2000 Compressibility effects in a turbulent annular mixing layer. part 1. turbulence and growth rate. *J. Fluid Mech.* **421**, 229–267.

Gad-el-Hak, M. & Blackwelder, R. F. 1987 Simulation of large-eddy structures in a turbulent boundary layer. *AIAA J.* **25** (9), 1207–1215.

Gardner, P. J., Roggemann, M. C., Welsh, B. M. & Bowersox, R. D. 1995 Statistical assessment of optical phase fluctuations through turbulent mixing layers. In *Optical Techniques in Fluid, Thermal and Combustion Flow* (ed. S. S. Cha & J. D. Trollinger), vol. 2546. SPIE.

Ghoniem, A. F. 1990 Vortex simulation of reacting shear flow. In *Numerical Approaches to Combustion Modeling* (ed. E. S. Oran & J. P. Boris), vol. 135, pp. 305–348. American Institute of Aeronautics and Astronautics.

Ghoniem, A. F., Heidarinejad, G. & Krishnan, A. 1988 Numerical simulation of a thermally stratified shear layer using the vortex element method. *J. Comput. Phys.* **79**, 135–166.

Gilbert, K. G. 1982 Overview of aero-optics. In *Aero-Optical Phenomena* (ed. K. G. Gilbert & L. J. Otten), vol. 80, pp. 1–9. American Institute of Aeronautics and Astronautics.

Goldstein, R. J. (Ed.) 1983 *Fluid Mechanics Measurements*. Hemisphere.

Gordeyev, S., Jumper, E. J., Ng, T. T. & Cain, A. B. 2003 Aero-optical characteristics of compressible, subsonic turbulent boundary layers. *AIAA Paper* 2003-3606.

Gross, K. P., McKenzie, R. L. & Logan, P. 1987 Measurements of temperature, density, pressure, and their fluctuations in supersonic turbulence using laser-induced fluorescence. *Exps. Fluids* **5**, 372–380.

Hall, J. L., Dimotakis, P. E. & Rosemann, H. 1993 Experiments in nonreacting compressible shear layers. *AIAA J.* **31**, 2247–2254.

Havener, G. & Heltsley, F. 1994 Design aspects and preliminary holographic-PIV measurements for a subsonic free shear layer flow channel. *AIAA Paper* 94-2550.

Hedges, L. S. & Eberhardt, D. S. 1993 Comparison of confined, compressible, spatially developing mixing layers with temporal mixing layers. *AIAA J.* **31** (11), 1977–1983.

Hilsch, R. 1946 The use of the expansion of gases in a centrifugal field as cooling process. *Rev. Sci. Instrum.* **18**, 108–113.

Holden, M. S., Parker, R. A., Walker, B. J., Lutz, S. & Smolinski, G. J. 2000 Ground tests of aerothermal and aero-optical characteristics of full-scale AIT and SM BLK IVA interceptors at fully duplicated flight conditions. *AIAA Missile Sciences Conference, Monterey, CA.*

Hugo, R. J. 1995 Quantifying the spatio-temporal effects of optically-active turbulent flowfields on a coherent optical wave. PhD thesis, University of Notre Dame, Notre Dame, Indiana.

Hugo, R. J. & Jumper, E. J. 1996 Experimental measurement of a time-varying optical path difference by the small-aperture beam technique. *Appl. Optics* **35** (22), 4436–4447.

Hugo, R. J., Jumper, E. J., Havener, G. & Stepanek, C. 1995 Time-resolved aero-optical measurements of a wavefront aberrated by a compressible free shear layer. *AIAA Paper* 95-1979.

Hugo, R. J., Jumper, E. J., Havener, G. & Stepanek, C. 1997 Time-resolved wave front measurements through a compressible free shear layer. *AIAA J.* **35**, 671–677.

Hugo, R. J. & McMackin, L. 1996 Conditionally sampled two-dimensional optical wavefront measurements in the near-nozzle region of a heated axisymmetric jet. In *Image Propagation through the Atmosphere* (ed. J. C. Dainty & L. R. Bissonnette), vol. 2828, pp. 50–61. SPIE.

Inoue, O. 1985 Vortex simulation of a turbulent mixing layer. *AIAA J.* **23**, 367–373.

de Jonckheere, R. K., Chou, D. C., Walker, J. & Miller, D. J. 1988 Large-scale turbulence structuring in high Reynolds number flows. *AIAA Paper* 88-3671.

Jones, B. G., Adrian, R. J., Nithianandan, C. K. & Planchon Jr., H. P. 1979 Spectra of turbulent static pressure fluctuations in jet mixing layers. *AIAA J.* **17**, 449–457.

Jumper, E. J. & Fitzgerald, E. J. 2001 Recent advances in aero-optics. *Prog. Aerospace Sci.* **37**, 299–339.

Jumper, E. J. & Hugo, R. J. 1995 Quantification of aero-optical phase distortion using the small-aperture beam technique. *AIAA J.* **33**, 2151–2157.

Kistler, A. L. 1959 Fluctuation measurements in a supersonic turbulent boundary layer. *Phys. Fluids* **2**, 290.

Kistler, A. L. & Chen, W. S. 1963 The fluctuating pressure field in a supersonic turbulent boundary layer. *J. Fluid Mech.* **16**, 41–64.

Koochesfahani, M., Cohn, R. & MacKinnon, C. 2000 Simultaneous whole-field measurements of velocity and concentration fields using a combination of MTV and LIF. *Meas. Sci. Techn.* **11**, 1289–1300.

Kovasnay, L. S. G. 1950 Hot wire anemometer in supersonic flow. *J. Aeronaut. Sci.* **17**, 565–572.

Kuethe, A. M. & Chow, C. 1998 *Foundations of Aerodynamics*, 5th edn. John Wiley & Sons.

Kurosaka, M. 1982 Acoustic streaming in swirling flow and the Ranque-Hilsch (vortex-tube) effect. *J. Fluid Mech.* **124**, 139–172.

Leep, L. J., Dutton, J. C. & Burr, R. F. 1993 Three-dimensional simulations of compressible mixing layers: Visualizations and statistical analysis. *AIAA J.* **31**, 2039–2046.

Lele, S. K. 1994 Compressibility effects on turbulence. In *Annu. Rev. Fluid Mech.* **26**, 211–254.

Leonard, A. 1980 Vortex methods for flow simulation. *J. Comput. Phys.* **37**, 289–335.

Liou, T., Lien, W. & Hwang, P. 1995 Compressibility effects and mixing enhancement in turbulent free shear flows. *AIAA J.* **33**, 2332–2338.

Luna, T., Truman, C. R. & Masson, B. S. 1997 Linear stochastic estimation of optical beam deflection through a heated jet. *AIAA Paper* 97-0072.

Lutz, S. A. 1989 Modeling of density fluctuations in supersonic turbulent boundary layers. *AIAA J.* **27**, 822–823.

Malley, M., Sutton, G. W. & Kincheloe, N. 1992 Beam-jitter measurements of turbulent aero-optical path differences. *Appl. Optics* **31**, 4440–4443.

Masson, B., McMackin, L., Wissler, J. & Bishop, K. 1995 Study of a round jet using a Shack-Hartmann wavefront sensor. *AIAA Paper* 95-0644.

McMackin, L., Hugo, R. J., Pierson, R. E. & Truman, C. R. 1997 High speed optical tomography system for imaging dynamic transparent media. *Optics Express* **1** (11), 302–311.

McMackin, L., Masson, B., Clark, N., Bishop, K., Pierson, R. & Chen, E. 1995 Hartmann wave front sensor studies of dynamic organized structure in flowfields. *AIAA J.* **33**, 2158–2164.

Meier, H. U. & Rotta, J. C. 1971 Temperature distributions in supersonic turbulent boundary layers. *AIAA J.* **9**, 2149–2156.

Michalke, A. 1965 On spatially growing disturbances in an inviscid shear layer. *J. Fluid Mech.* **23**, 521–544.

Morkovin, M. V. 1962 Effects of compressibility on turbulent flows. In *Mécanique de la Turbulence* (ed. A. Favre), pp. 367–380. Paris: CNRS.

Oh, C. K. & Loth, E. 1995 Unstructured grid simulations of spatially evolving supersonic shear layers. *AIAA J.* **33**, 1229–1238.

Oljaca, M. & Glezer, A. 1997 Measurements of aero-optical effects in a plane shear layer. *AIAA Paper* 97-2352.

Olsen, M. G. & Dutton, J. C. 1999 Planar velocity measurements in a weakly compressible mixing layer. *AIAA Paper* 99-3584.

Papamoschou, D. & Roshko, A. 1986 Observations of supersonic free shear layers. *AIAA Paper* 86-0162.

Papamoschou, D. & Roshko, A. 1988 The compressible turbulent shear layer: An experimental study. *J. Fluid Mech.* **197**, 453–477.

Rose, W. C. 1978 Measurements of aerodynamic parameters affecting optical performance. *Tech. Rep.* AFWL-TR-78-191. Air Force Weapons Laboratory, Kirtland AFB, NM.

Rose, W. C. & Johnson, D. A. 1982 Unsteady density and velocity measurements in the 6 × 6 ft wind tunnel. In *Aero-Optical Phenomena* (ed. K. G. Gilbert & L. J. Otten), vol. 80, pp. 218–232. American Institute of Aeronautics and Astronautics.

Rose, W. C., Johnson, D. A. & Otten, L. J. 1982 Summary of ALL Cycle II.5 aerodynamic shear- and boundary-layer measurements. In *Aero-Optical Phenomena*(ed. K. G. Gilbert & L. J. Otten), vol. 80, pp. 295–305. American Institute of Aeronautics and Astronautics.

Rosenhead, L. 1932 The formation of vortices from a surface discontinuity. *Proc. R. Soc. Lond.* A **134**, 170–192.

Samimy, M. & Elliott, G. S. 1990 Effects of compressibility on the characteristics of free shear layers. *AIAA J.* **28**, 439–445.

Sandham, N. D. & Reynolds, W. C. 1990 Compressible mixing layer: Linear theory and direct simulation. *AIAA J.* **28**, 618–624.

Sandham, N. D. & Reynolds, W. C. 1991 Three-dimensional simulations of large eddies in the compressible mixing layer. *J. Fluid Mech.* **224**, 133–158.

Schlichting, H. 1979 *Boundary-Layer Theory*, 7th edn. McGraw-Hill.

Shyy, W. & Krishnamurty, V. S. 1997 Compressibility effects in modeling complex turbulent flows. *Prog. Aerospace Sci.* **33**, 587–645.

Smith, D. R. & Smits, A. J. 1993 Simultaneous measurement of velocity and temperature fluctuations in the boundary layer of a supersonic flow. *Exp. Thermal Fluid Sci.* **7**, 221–229.

Smits, A. J. & Dussauge, J.-P. 1996 *Turbulent Shear Layers in Supersonic Flow*. American Institute of Physics.

Southwell, W. H. 1980 Wave-front estimation from wave-front slope measurements. *J. Optical Soci. of Am.* **70**, 998–1006.

Thomas, F. O. 1991 Structure of mixing layers and jets. *Appl. Mech. Rev.* **44**, 119–153.

Tsai, Y. P. & Christiansen, W. H. 1990 Two-dimensional numerical simulation of shear-layer optics. *AIAA J.* **28**, 2092–2097.

Vreman, B., Geurts, B. & Kuerten, H. 1997 Large-eddy simulation of the turbulent mixing layer. *Journal Fluid Mechanics* **339**, 357–390.

Weston, C. P. 1982 Influence of periodic compressible vortices on laser beam intensity. Master's thesis, AFIT/GAE/AA/82D-32, Air Force Institute of Technology.

Weston, C. P. & Jumper, E. J. 2002 Influence of periodic compressible vortices on laser beam intensity. *AIAA Paper* 2002-2276.

White, F. M. 1991 *Viscous Fluid Flow*, 2nd edn. McGraw-Hill.

Winant, C. D. & Browand, F. K. 1974 Vortex pairing: The mechanism of turbulent mixing-layer growth at moderate Reynolds number. *J. Fluid Mech.* **63**, 237–255.

Wygnanski, I. & Oster, D. 1982 The forced mixing layer between parallel streams. *J. Fluid Mech.* **123**, 91–130.